



Virginia Commonwealth University
VCU Scholars Compass

Theses and Dissertations

Graduate School

2018

Synthesis and Analysis of Gold Nanoclusters

Patrick Woodworth
Virginia Commonwealth University

Follow this and additional works at: <https://scholarscompass.vcu.edu/etd>

© The Author

Downloaded from

<https://scholarscompass.vcu.edu/etd/5569>

This Dissertation is brought to you for free and open access by the Graduate School at VCU Scholars Compass. It has been accepted for inclusion in Theses and Dissertations by an authorized administrator of VCU Scholars Compass. For more information, please contact libcompass@vcu.edu.

Synthesis and Analysis of Gold Nanoclusters

A dissertation submitted in partial fulfillment of the requirements for the degree of
Doctor of Philosophy in Nanoscience and Nanotechnology at
Virginia Commonwealth University.

By

Patrick Harold Woodworth
Bachelors of Science, SUNY Cortland, 1997
Masters of Science, Virginia Commonwealth University, 2002

Director: Dr. Massimo Bertino, Professor, Department of Physics

Virginia Commonwealth University
Richmond, Virginia
May 2018

Acknowledgment

The completion of this dissertation is the culmination of many years of work and would not be possible without the love and support of all the people around me. I would especially like to thank Dr. Massimo Bertino for all his guidance, support and understanding during this time. Secondly, I would like to thank Dr. Wijesinghe for allowing me access to his equipment, which proved invaluable for my work. I would also like to thank Dr. Reiner and Dr. Demchenko for providing support and agreeing to serve on my committee.

Lastly, I would like to dedicate this work to my loving wife Kara and our wonderful son Nicholas. Their support over the years helped to keep me motivated and focused, allowing me to accomplish this dream of mine.

Thank you.

TABLE OF CONTENTS

List of Figures	vi
Abstract	xvi
Chapter 1: Introduction	1
1.1 Gold Nanoparticles in History	2
1.2 Synthesis Methods	3
1.3 Applications	5
1.4 Monodispersity and Size Control.....	8
1.5 Thiol protected clusters.....	9
1.6 Phosphine protected clusters.....	14
1.7 Nanopores and Sensing.....	19
1.8 Nucleation of Clusters.....	20
Chapter 2: Experimental Analytical Methods.....	24
2.1 Electrospray Ionization Mass Spectrometry	25
2.2 Ultraviolet – Visible Spectroscopy	31
2.3 Transmission Electron Microscopy	33
2.4 X-Ray Techniques	35
Chapter 3: Synthesis of gold clusters with flexible and rigid diphosphine ligands and the effect of spacer and solvent on the size selectivity	37
3.1 Introduction.....	38
3.2 Results and Discussion	42
3.2.1 L^1 Au Clusters	42
3.2.2 L^3 Au Clusters	44
3.2.3 L^4 Au Clusters	45
3.2.4 L^6 Au Clusters	46
3.2.5 L^{Ar} Au Clusters	49
3.2.6 L^{Bn} Au Clusters	51
3.2.7 L^{Bp} Au Clusters	52
3.3 Experimental.....	53
3.3.1 Measurements	54
3.4 Conclusions	54

Chapter 4: Synthesis of Diphosphine Ligated Au ₈ and Au ₁₄ Nanoclusters	56
4.1 Introduction.....	57
4.2 Experimental Section	58
4.3 Results and Discussion	60
4.4 Conclusion	62
4.5 Supporting Information.....	62
4.5.1 Characterization	62
Chapter 5: Novel Methods for the Synthesis of Monodisperse Au ₉ solutions and Au films through the addition of NiCl ₂	65
5.1 Introduction.....	66
5.2 Experimental Procedures	67
5.3 Results and Discussion	67
5.4 Conclusion	71
Chapter 6: Nanopore investigation of the <i>p</i> -mercaptobenzoic acid ligated gold nanocluster (Au _x <i>p</i> -MBA _y).....	72
6.1 Introduction.....	73
6.2 Methods.....	73
6.3 Results.....	74
6.4 Conclusion	74
Chapter 7: Summary	76

LIST OF FIGURES

Figure 1.1: The Lycurgus cup – displays a different color depending on whether it is illuminated externally (a) or internally (b).....	2
Figure 1.2: Electron micrograph of a gold sol reduced with sodium citrate (standard citrate sol) magnification 50,000 diameters. Taken from <i>Turkevich</i>	3
Figure 1.3: Brust Synthesis of Thiol-derivatised Gold Nanoparticles in a Two-phase Liquid-Liquid.....	4
Figure 1.4: Turn over frequencies and band-gap measured by STM as a function of the diameter of Au islands deposited on TiO_2	5
Figure 1.5: Dark field light scattering images of cytoplasm and nuclear targeting AuNPs. a) RGD-AuNPs located in the cytoplasm of cancer cells. b) RGD/NLS-AuNPs located at the nucleus of cancer cells. c) RGD AuNPs located in the cytoplasm of normal cells. d) RGD/NLS-AuNPs located at the nucleus of normal cells. The cancer and normal cells were incubated in the presence of these AuNPs at a concentration of 0.4 nM for 24 hours and these images clearly display the efficient uptake of AuNPs in cancer cells compared with normal cells. Scale bar 10 μm	7
Figure 1.6: Solutions of gold colloids increasing in size.....	8
Figure 1.7: UV-Visible Spectrum of increasing gold nanoparticles spheres.....	9
Figure 1.8: PAGE separated Au:SG gold nanomolecules. Photograph of (a) 35% gel showing separation of smaller nanomolecules in bands 0–13; (b) 23% gel showing separation of larger nanomolecules in bands 14–25; (c) cut and crushed gel bands in vials; and (d) extracted nanomolecules dissolved in water. From Size-dependent molecule-like to plasmonic transition in water-soluble glutathione stabilized gold nanomolecules	10
Figure 1.9: Crystal structure of $\text{Au}_{25}(\text{SR})_{18}$ cluster. A) the icosahedral Au_{13} core, B) the Au_{13} core plus the exterior 12 Au atoms, C) the whole Au_{25} cluster protected by 18 thiolate ligands (only S shown in yellow).....	11
Figure 1.10: UV-Vis spectrum of Au_{25} clusters	11
Figure 1.11: (A) Kohn–Sham orbital energy level diagram for a model compound $\text{Au}_{25}(\text{SH})_{18}$. Each KS orbital is drawn to indicate the relative contributions (line length with color labels) of the atomic orbitals of Au (6sp) in green, Au (5d) in blue, S (3p) in orange, and others in gray (those unspecified atomic orbitals, each with a < 1% contribution). The left column of the KS orbitals shows the orbital symmetry (g, u) and degeneracy (in parentheses); the right column shows the	

HOMO and LUMO sets. (B) The theoretical absorption spectrum of $\text{Au}_{25}(\text{SH})_{18}$. Peak assignments: peak (a) corresponds to 1.8 eV (observed), peak (b) corresponds to 2.75 eV (observed), and peak (c) corresponds to 3.1 eV (observed).	12
Figure 1.12: (A) Reversible conversion between the neutral and anionic $\text{Au}_{25}(\text{SR})_{18}$ nanoclusters. (B) DFT calculated Kohn–Sham orbital level diagram for the neutral and anionic nanoclusters, respectively. (C–D) Views of the highest occupied Kohn–Sham orbital for $[\text{Au}_{25}(\text{SH})_{18}]^0$ at the LB94//Xa/TZP level of theory. The HOMO possesses two lobes and exhibits distinct P-like character. (D) is rotated relative to (C) to show one of the lobes (contributed by three Au atoms in the icosahedral shell). (Purple: Au, yellow: S, white: H atoms).	13
Figure 1.13: Room temperature <i>IV</i> characteristics of an individual $\text{Au}_{55}(\text{PPh}_3)_{12}\text{Cl}_6$ cluster indicating a well-expressed Coulomb blockade	15
Figure 1.14: STM image of an individual $\text{Au}_{55}(\text{PPh}_3)_{12}\text{Cl}_6$ cluster at 7 K under UHV conditions together with a full-space model; the light dots indicate phenyl rings; the positions a and b indicate where the measurements have been performed to yield the <i>IV</i> characteristics.....	15
Figure 1.15: $[\text{Au}_{20}(\text{PP}_3)_4]\text{Cl}_4$ structure (left) , Mass spec indicating formation of monodisperse Au_{20} (right).....	16
Figure 1.16: Mass spec of L^3 , L^5 and L^6 ligated Au clusters (left), UV-Vis comparison of the same ligands (right).....	18
Figure 1.17: (left) α -hemolysin nanopore, (center) ionic current blockades, (right) multistate current blockades	19
Figure 1.18: a) LaMer’s mechanism describing the nucleation process: 1. rapid increase in molecular concentration, 2. the formation of stable clusters, 3. decrease in molecular material due to nucleation. b) Graph of cluster free energy vs. cluster radius according to classical nucleation theory. The critical radius r^* and critical activation energy ΔG^* for stable clusters are shown.....	21
Figure 2.1: a. Picture of the 3 major steps of ESI in the atmospheric pressure region run in positive ion mode. b. Picture of an electrospray ion source and mass spectrometer. Sample is inserted via the syringe.....	25
Figure 2.2: The mechanism for electrospray ionization	26
Figure 2.3: Picture of the quadrupole device (QMF).....	29
Figure 2.4: Possible electron transistions. Taken from chemistry.msu.edu	31

Figure 3.1: Pictures of, a) 1,1-Bis(diphenylphosphino)methane, b) 1,3-Bis(diphenylphosphino)propane, c) 1,4-Bis(diphenylphosphino)butane, d) 1,6-Bis(diphenylphosphino)hexane, e) Xantphos (rigid spacer), f) 2,2'-Bis(diphenylphosphino)-1,1'-binaphthyl (Binap), g) 2,2'-Bis(diphenylphosphino)biphenyl	41
Figure 3.2: UV-Visible Spectroscopy of Au:L ¹	43
Figure 3.3: ESI-MS of L ¹ in a) butanol, b) chloroform and c) methanol	43
Figure 3.4: UV-Visible Spectroscopy of Au:L ³ . The 420 nm peak is present in all solvents indicating the formation of Au ₁₁ and the size selective behavior of L ³	44
Figure 3.5: ESI-MS of Au:L ³ showing Au ₁₁ along with smaller gold complexes prepared in chloroform.....	44
Figure 3.6: UV-Visible Spectroscopy of Au:L ⁴	45
Figure 3.7: ESI-MS of L ⁴ in a) butanol and b) methanol	45
Figure 3.8: a) ESI-MS of L ⁴ in chloroform. b) An expanded view of L ⁴ in chloroform showing the 1450 m/z to 2000 m/z highlighting the Au ₁₂ , Au ₁₀ and Au ₈ clusters.....	46
Figure 3.9: a) UV-Visible Spectroscopy of Au:L ⁶ . b) An expanded view of the chloroform and methanol mix showing the 414 nm and 476 nm peaks corresponding to Au ₁₀ and Au ₈ , respectively	47
Figure 3.10: ESI-MS of L ⁶ in a) butanol and b) methanol	48
Figure 3.11: a) ESI-MS of L ⁶ in chloroform. b) An expanded view of L ⁶ in chloroform showing the 1400 m/z to 2000 m/z highlighting the Au ₁₀ cluster.....	48
Figure 3.12: UV-Visible Spectroscopy of Au:L ^{Ar}	49
Figure 3.13: ESI-MS of L ^{Ar} (Xantphos) in Chloroform a) and Methanol b) and c).....	49
Figure 3.14: Time study of UV-Visible Spectroscopy of Au:L ^{Ar} showing the instability of Xantphos	50
Figure 3.15: ESI-MS of L ^{Ar} (Xantphos) in chloroform a) immediate (< 4 hrs) and b) 1 month old sample showing the lack of size selectivity and instability of Xantphos.....	50
Figure 3.16: UV-Visible Spectroscopy of Au:L ^{Bn} . On the right is an expanded view of chloroform showing the 380 nm and 430 nm peaks corresponding to Au ₉ and Au ₁₀ , respectively	51
Figure 3.17: ESI-MS of L ^{Bn} in Chloroform a) and Methanol b) and c). Expanded view in Methanol c)	52
Figure 3.18: UV-Visible Spectroscopy of Au:L ^{Bp}	53

Figure 3.19: ESI-MS of L^{Bp} in Chloroform a) and Butanol b) and c). Expanded view in Butanol c)	53
Figure 4.1: Optical absorption spectra of the parent Au_{11} suspension and of the same suspension after addition of $MnCl_2$. The shift in peaks from 420 nm to 505 nm indicates the transformation of $[Au_{11}L^3_5]^{3+}$ to $[Au_8L^3_4Cl_2]^{2+}$ and $[Au_{14}L^3_5Cl_4]^{2+}$	61
Figure 4.2: (Left) ESI-MS of our suspension after 3 weeks for $[Au_8L^3_4Cl_2]^{2+}$ and $[Au_{14}L^3_5Cl_4]^{2+}$. (Middle and Right) The experimental and simulated isotopic patterns of the Au_8 and Au_{14} clusters	61
Figure 4.3: ESI-MS over 3-week period showing the growth of the 1647 m/z peak for Au_8	61
Figure 4.S1: a) Bright field micrographs showing the presence of aggregates with a diameter < 2 nm. b) EELS measurements showing peaks characteristic of Mn corresponding to the $L_{2,3}$ edges. Au could not be measured by EELS because its lines lie outside the maximum energy accessible to our analyzer (1000 eV). The lines around 500 eV are characteristic of adventitious oxygen and are routinely encountered in samples analyzed with our microscope, including, for example, pure Au.....	63
Figure 4.S2: XPS analysis of films produced by evaporation of the solution on silicon	64
Figure 4.S3: VSM analysis of films produced by evaporation of the solution on silicon.....	64
Figure 5.1: (a) UV-Vis spectra of gold film (yellow) and gold-nickel film (blue). Both have peaks at ~600 nm. (b) Shows UV-Vis for the Au:Ni solution. We can see a peak at 420 nm and one at 520 nm. This is consistent with Au_8 and Au_9 cores.....	68
Figure 5.2: ESI-MS of the gold nickel solution after 1 day and 4 days reveals an evolution of the 1935 m/z peak	68
Figure 5.3: ESI-MS of the gold plating solution	69
Table 5.1: Measurements of resistivity with decreasing temperature.....	69
Figure 5.4: (left)TEM image of AuNi plated onto a grid. (right) TEM Nickel map. Scale bars are 20 nm	70
Figure 5.5: EELS of Nickel line	70
Figure 5.6: XRD showing the evolution of Au (38°) and Ni (44°) peaks with increasing temperature	70
Figure 5.7: UV-Vis spectra of $KAuCl_4$ and $NiCl_2$ co-reduced with L^3 over time. We can see the 420 nm peak which we have shown is evidence of the Au_{11} cluster	71

Figure 6.1: Schematic illustration of the experimental setup and a typical current trace for a single 4-MBA capped cluster trapped in the α HL pore. (A) A micropipette tip filled with a preformed sample of $\text{Au}_x(4\text{-MBA})_y$ nanoparticles is positioned near the cis-side entry of an α HL pore. (B) Time trace for a typical capture experiment shows that after applying a sufficient voltage and a 30-second delay, a constant backing pressure is applied to eject particles near the pore. Upon entry and capture of a particle into the pore, the current is reduced ca. 25% and the ejection pressure is immediately zeroed. (C) A low pass filter ($f_c = 100$ Hz) is used to extract step-like current noise indicative of events. Data shown was taken in 3M KCl at pH 7.2 under an applied 70 mV transmembrane potential.75

Figure 6.2: (A) Typical blockade current from a 4-MBA capped cluster shows discrete steps and ten clear substates. (B) An all-points histogram of this current identifies the quantized nature of the current states and the spacing shows a nearly linear dependence on the state and the steps. (C) The distribution of steps (transitions) between states shows that the events are caused by nearest state transitions or “next-nearest” state transitions.75

Abstract

SYNTHESIS AND ANALYSIS OF GOLD NANOCCLUSERS

By Patrick H. Woodworth, Ph.D.

A dissertation submitted in partial fulfillment of the requirements for the degree of Doctor of Philosophy in Nanoscience and Nanotechnology at Virginia Commonwealth University.

Virginia Commonwealth University, 2018

Major Director: Dr. Massimo Bertino
Professor of Physics

Gold Nanoclusters are of particular interest due to their many possible applications across a wide range of scientific fields. More specifically, nano-sized gold particles have potential to be used in drug delivery systems, cancer therapy and catalysis. This dissertation focuses on improving our understanding of ligated gold nanoclusters by examining the role of a variety of phosphine based ligands, novel methods to produce monodisperse solutions, and investigating the kinetics of water soluble ligated gold nanoclusters.

The addition of ligands to solutions of Au have shown to produce small (< 20 Au atoms) clusters. All nanocluster solutions were prepared in a similar manner. Typically, a gold salt, either Chloro(triphenylphosphine) gold(I) ($\text{Au}(\text{PPh}_3)\text{Cl}$), or Potassium gold (III) chloride (KAuCl_4), were dissolved in various solvents. Next, an equal concentration of ligand was added to the solution and stirred until completely dissolved. Finally, all were reduced with 5X the concentration of borane-*tert*-butylamine (BTBC) after which were sonicated for ~20 minutes. The timing and method of adding the ligands and reducing agent varied depending on the solution and solubility of the ligands.

Primarily we used Electrospray Ionization Mass Spectrometry (ESI-MS) and Ultraviolet – Visible Spectroscopy (UV-VIS) for the characterization of samples, however, occasionally

Transmission Electron Microscopy (TEM), X-Ray Diffraction (XRD) and X-Ray Photoemission Spectroscopy (XPS) were used. The most recent research took advantage of the size selective nature of an alpha hemolysin (α -HL) nanopore to investigate the kinetics of thiol-ligated Au clusters ~ 2 nm in size.

The relationship between ligand rigidity and solvent polarity and the size and dispersity of Au cluster suspensions was investigated. We observed the formation of stable monodisperse clusters with the shortest ligand, (L^3), independent of solvent. With a longer flexible ligand, (L^6), we observed primarily Au_{8-10} cores depending on the ratio of L^6/PPh_3 . All other ligands yielded polydisperse distributions. These dispersions contained clusters with a nuclearity between 8 and 11, for example $[Au_{10}(PPh_3)_9]^{3+}$ in L^{Bn} and $[Au_8(PPh_3)_7]^{2+}$ in L^{Bp} , were observed in the initial stages, but they were not stable and precipitated out or plated the glass vial. We also observed that the polarity of the solvent did not play a significant role in the formation of MPC's, however a correlation between the size of the solvent and MPC formation was observed.

The growth and evolution of two unique gold structures was also observed via UV-Vis and ESI-MS. Solutions were prepared which contained Potassium gold (III) chloride and $PPh_2(CH_2)_3PPh_2$, i.e., 1,3-bis(diphenylphosphino)propane, denoted by L^3 , reduced with Borane tert-butylamine complex (BTBC) in a 1:1 diethyl ether:methanol mix, which yielded a stable $[Au_{11}(L^3)_5]^{+3}$. Starting with this known Au_{11} solution, the addition of Mn^{2+} has shown to lead to the formation of a stable diphosphine ligated Au_8 and a new Au_{14} species.

Additionally, we show that the co-reduction of $NiCl_2$ and Au in the absence of the ligand (L^3) does give us a simple method for the production of a monodisperse $[Au_9(PPh_3)_8]^{2+}$ cluster solution and via electroless deposition does give us a potential low temperature pathway to the formation of a AuNi nanoalloy particle.

CHAPTER 1: Introduction

1 Introduction

1.1 Gold Nanoparticles in History

The history of gold nanoparticles dates back to the 5th or 4th century BC in Egypt and China. Early examples of gold colloid use are to make ruby and purple glass for coloring ceramics and making stained glass.¹ One of the most famous examples is seen in Figure 1.1, the Lycurgus cup (4th century AD), whose glass changes from an opaque green (reflected light) to a translucent red from transmitted light. This color change is due to the Ag and Au colloids present in the glass (Dichroic glass). Analysis has shown that the nanoparticles are in the range of 50-100 nm.² Early uses for gold nanoparticle also include potential medical benefits. In China ~2500 BC, it has been reported use of gold to heal fistulas and haemorrhoids^{1,2}. In medieval times, (with the discovery of aqua regia), it was used to treat melancholy, fainting and fevers as well as in the 19th century, syphilis¹. Solutions of colloidal gold were also used as tonics and elixirs, especially in combination with alcohol. Colloidal gold is still applied to treat arthritis³. Scientific research with AuNP's is much more recent, beginning with Faraday in 1857. Faraday performed experiments on the synthesis and absorption of the ruby gold solution and was the first to correctly associate the color with the presence of gold.

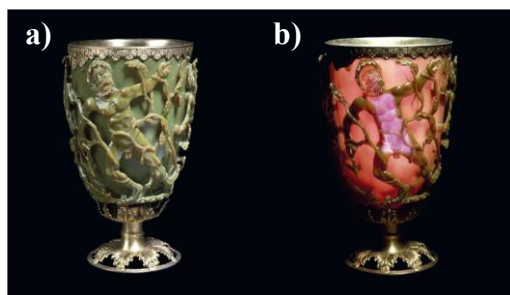


Figure 1.1: The Lycurgus cup – displays a different color depending on whether it is illuminated externally (a) or internally (b). Reproduced from Ref 1.

1.2 *Synthesis Methods*

There are many methods, both physical and chemical, that scientist use in the synthesis of nanoparticles and nanoclusters. This section focuses on the wet chemical synthesis introduced by Faraday, Turkevich and Brust-Schiffrin.

In 1857, Faraday reported the formation of deep red solutions of colloidal gold by reduction of an aqueous solution of chloroaurate (AuCl_4^-) using phosphorus in CS_2 (a two-phase system). He investigated the optical properties of thin films prepared from dried colloidal solutions and observed reversible color changes of the films upon mechanical compression (from bluish-purple to green upon pressurizing)¹.

In the 1950's John Turkevich developed a simple method to produce relatively monodisperse gold colloids using Chloroaurate acid reduced and stabilized with sodium citrate in water. After a few minutes, the wine-red colloidal suspension is obtained, and the AuNP size is about 20 nm (Figure 1.2). This method for producing nanoparticles has been regarded as the most popular method for a long time^{4,5}.

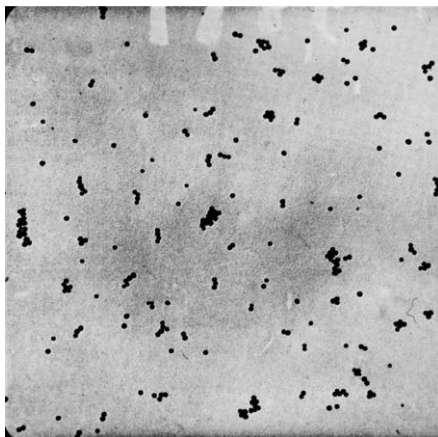


Figure 1.2: Electron micrograph of a gold sol reduced with sodium citrate (standard citrate sol) magnification 50,000 diameters⁴. Reproduced from Ref 4.

Brust and Schiffrin discovered a way to produce smaller AuNP's in toluene using HAuCl_4 and tetracyclammonium bromide (TOAB) reduced with Sodium Borohydrate. The two-phase Brust-Schiffrin method was the first method able to prepare the thiolate-stabilized AuNPs via *in situ* synthesis, and it has been met with great success^{6,7}. The method's high impact is due to its ease of synthesis in ambient condition, the relative high thermal and air stability of the AuNPs, the capability for isolation and re-dissolution without aggregation or decomposition, the ability to control size (less than 5 nm) with narrow dispersity, and the relatively easily functionalization and modification by ligand substitution. Relatively strong gold-sulfur bonds with diameters that are in the 2–5 nm range stabilize the AuNPs, and their shapes are cuboctahedral and icosahedral (Figure 1.3). Due to the nucleation-growth-passivation kinetics model by which the sulfur-containing agents inhibit the growth process, larger S/Au mole ratios give smaller average core sizes⁵.

1.3 Applications

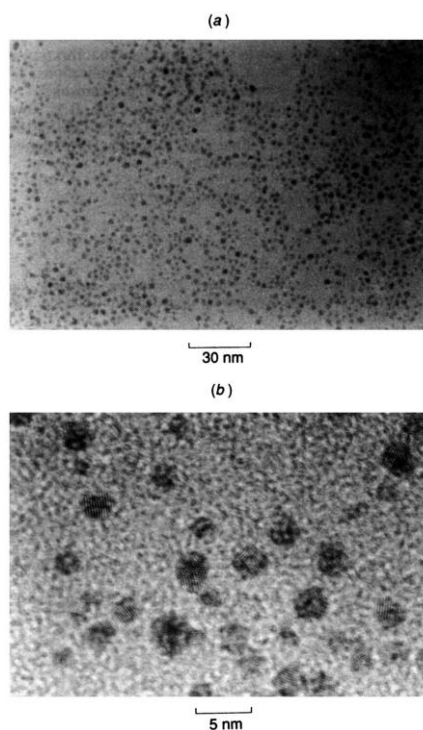


Figure 1.3: Brust Synthesis of Thiol-derivatised Gold Nanoparticles in a Two-phase Liquid-Liquid. Reproduced from Ref. 6 and 7.

Synthetic developments of monodisperse monolayer protected clusters (MPC's) are rapidly becoming an exciting area of research. Gold nanoparticles and nanoclusters exhibit optical properties that make them candidates for applications such as data storage, ultrafast switching and gas sensors⁸. Additionally, gold nanoclusters have the potential to be utilized in drug delivery systems, cancer therapy and treatment for Alzheimers disease, and for their use in catalysis⁹⁻¹².

Gold is historically known for being chemically inert. It is one of the most stable metals in the group 8 elements, and resistant to oxidation. In the 1970s, Parravano's group reported the investigation of the activity of gold in oxygen/hydrogen transfer reactions^{13,14} and the reduction of NO by dihydrogen, however these findings did not suggest gold as a superior catalyst. In 1989, the discovery by Haruta et al. that AuNPs supported on Co_3O_4 , Fe_2O_3 , or TiO_2 were highly active catalysts, under high dispersion, for CO and H_2 oxidation¹⁵, NO reduction¹⁶, water-gas shift reaction¹⁷, CO_2 hydrogenation¹⁸, and catalytic combustion of methanol¹⁹ (Figure 1.4). These discoveries were considered important by the chemical community and have begun renewed interest in the use of gold for catalysis. Catalysis with AuNPs, is now an expanding area, and a large number of new catalytic systems for various reactions are now being explored.

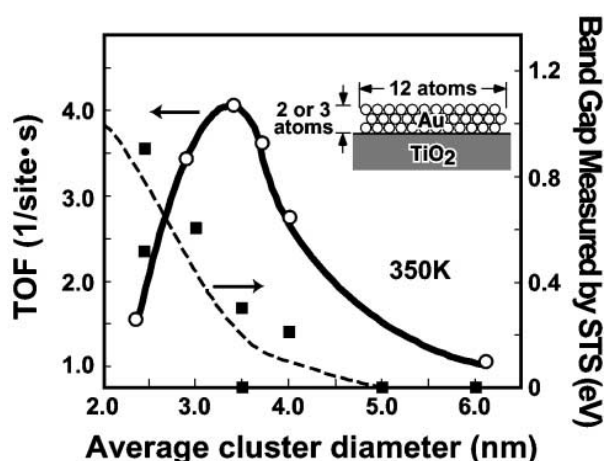


Figure 1.4: Turn over frequencies and band-gap measured by STM as a function of the diameter of Au islands deposited on TiO_2 . Reproduced from Ref 15.

A relatively new and very interesting area of cluster application is their use as cluster-assembled materials. Cluster assembled materials are solids in which clusters serve as the building blocks for larger materials. Following non-classical nucleation theory, these materials allow the integration of multiple length scales into an ordered material. The cluster properties change with size, composition, oxidation state, and the behaviors depend on their structure, which is why cluster assemblies are attracting interest in the forming of materials with novel combinations of properties. These materials help us to gain an understanding between the predictable size-invariant properties of solids and the properties observed at the nanometer scale. Recent synthetic advances confirm that the materials retain many of the characteristics of the original building blocks²⁰⁻²².

Lastly, gold nanoparticles are very promising for a wide range of biomedical applications such as molecular diagnosis, cellular imaging, and targeted therapy depending on the structure, composite and shape of the nanoparticles. Recently, AuNP's have been at the forefront of cancer research because of their facile synthesis and surface functionalization, strongly enhanced and tunable optical properties as well as their excellent biocompatibility for clinic settings²³. El Sayed et al. have also been able to selectively transport AuNP's into the cancer cell nucleus for imaging. To accomplish selectively transporting the AuNP's into the cancer cell nucleus, they conjugated arginine–glycine–aspartic acid peptide (RGD) and a nuclear localization signal peptide (NLS) to a 30-nm AuNP's via PEG²⁴. (Figure 1.5)

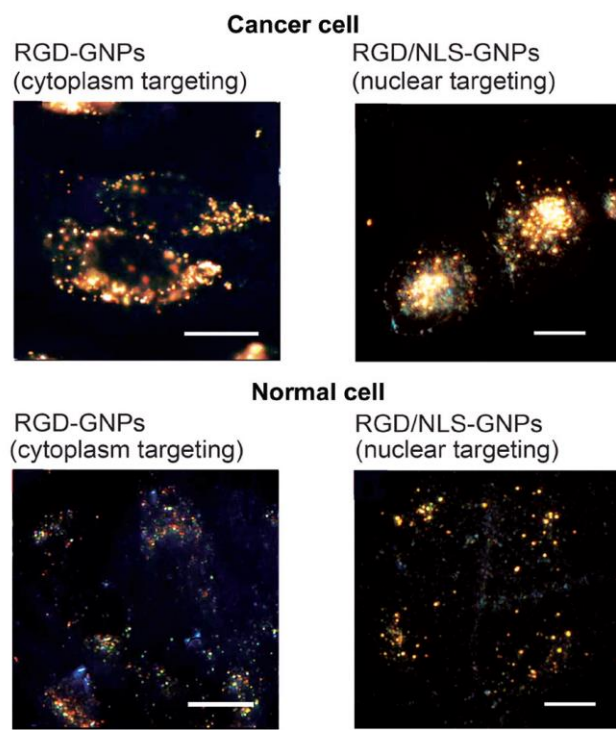


Figure 1.5: Dark field light scattering images of cytoplasm and nuclear targeting AuNPs. a) RGD-AuNPs located in the cytoplasm of cancer cells. b) RGD/NLS-AuNPs located at the nucleus of cancer cells. c) RGD AuNPs located in the cytoplasm of normal cells. d) RGD/NLS-AuNPs located at the nucleus of normal cells. The cancer and normal cells were incubated in the presence of these AuNPs at a concentration of 0.4 nM for 24 hours and these images clearly display the efficient uptake of AuNPs in cancer cells compared with normal cells. Scale bar 10 μ m. Reproduced from Ref. 24.

1.4 Monodispersity and Size Control

Unlike large gold nanoparticles, whose optical properties are dominated by surface plasmon resonances (SPR) due to excitation of electrons in the continuous conduction band, gold nanoclusters, exhibit discrete electronic structure and molecule-like properties, such as a HOMO-LUMO transition of a one-electron nature. The color of a gold colloidal solution was and is one of its most interesting properties. As we know, the color is attributed to the size and shape of the nanoparticles (Figure 1.6). This effect is a result of the Localized Surface Plasmon Band (LSPB) and can be explained by the collective oscillation of electrons of the conductive band near the Fermi level and where the absorption reaches a maximum at a certain wavelength. The location of the LSPB is characteristic for the material, the size, the shape, and the surrounding medium of a nanoparticle. The size distribution is so mirrored in the spectrum. Figure 1.7 shows a narrow size distribution causes a sharp LSPB, whereas a wide distribution reflects in a broad absorption band²⁵.

There are two main issues with the synthesis of gold nanoclusters. The first is the ability to synthesize monodisperse clusters, and the second is how to have direct control over the size of the clusters produced. Monodispersity and size control are essential in the formation of cluster

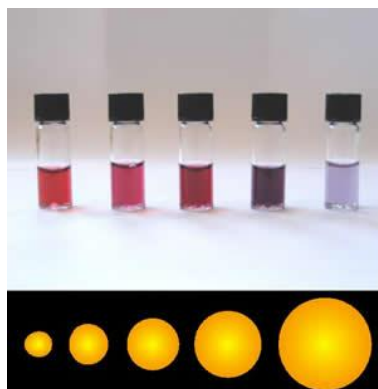


Figure 1.6: Solutions of gold colloids increasing in size

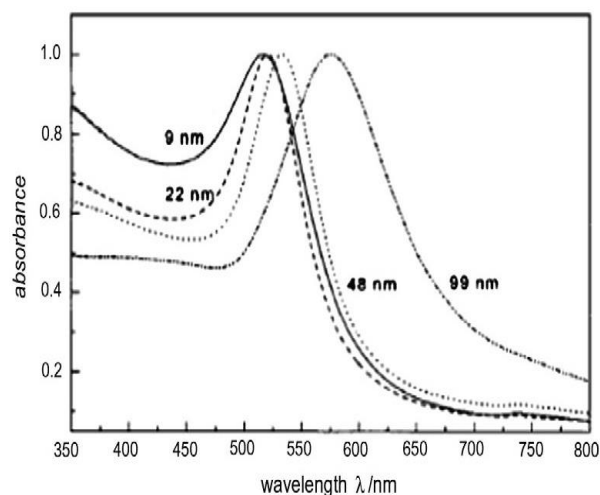


Figure 1.7: UV-Visible Spectrum of increasing gold nanoparticles spheres. Reproduced from Ref 25.

assembled materials and for use in practical applications. Recently, there have been many successful attempts answer these questions. The first is much simpler to resolve, as mentioned earlier, Turkevich in the 1950's developed a method to produce monodisperse gold nanoparticles. The following sections discuss a sample of what has been done to attain and explain monodisperse nanoclusters. In this work, I am going to concentrate on a few select clusters in both the thiol and phosphine protected cluster categories.

1.5 Thiol protected clusters

Thiolate-protected gold clusters are a type of stable ligand-protected metal cluster, synthesized from gold ions and thin layer compounds that play a special role in cluster physics because of their unique stability and electronic properties. Thiolate-protected gold clusters are achieved by the reduction of gold salt solutions, using a reducing agent in the presence of thiol compounds. There are several synthesis that exist which are similar to the Brust synthesis of colloidal gold, however the mechanism is not yet fully understood. The process produces a mixture

of dissolved, thiolate-protected gold clusters of different sizes. These particles can be separated by polyacrylamide gel electrophoresis (PAGE)²⁶. Monodisperse stable particles can be obtained if the synthesis is performed in a kinetically controlled manner, avoiding further separation steps. Refinement of these methods over the years have enabled scientists to produce high-quality synthesis of a few particularly stable “magic” compounds in the size range 1–3 nm, and a few have been determined up to molecular precision; these include $\text{Au}_{20}(\text{SR})_{16}$, $\text{Au}_{25}(\text{SR})_{18}$, $\text{Au}_{38}(\text{SR})_{24}$, $\text{Au}_{68}(\text{SR})_{34}$, $\text{Au}_{102}(\text{SR})_{44}$, and $\text{Au}_{144}(\text{SR})_{60}$.^{26–30} Various other thiolates have also been used for synthesis, including water soluble glutathione and *para* mercaptobenzoic acid and organic soluble alkylthiolates and phenylethanethiolates²⁷. (Figure 1.8)

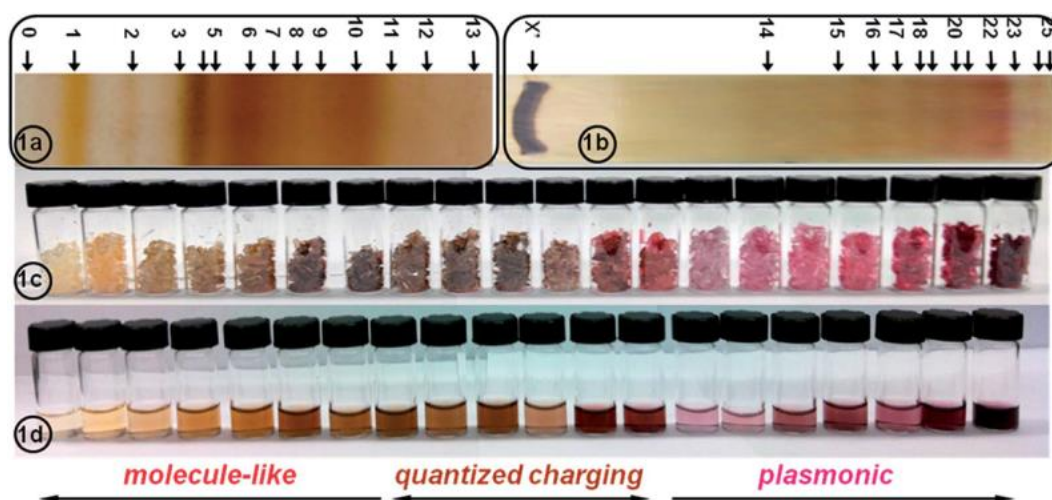


Figure 1.8: PAGE separated Au:SG gold nanomolecules. Photograph of (a) 35% gel showing separation of smaller nanomolecules in bands 0–13; (b) 23% gel showing separation of larger nanomolecules in bands 14–25; (c) cut and crushed gel bands in vials; and (d) extracted nanomolecules dissolved in water. From Size-dependent molecule-like to plasmonic transition in water-soluble glutathione stabilized gold nanomolecules. Reproduced from Ref. 25.

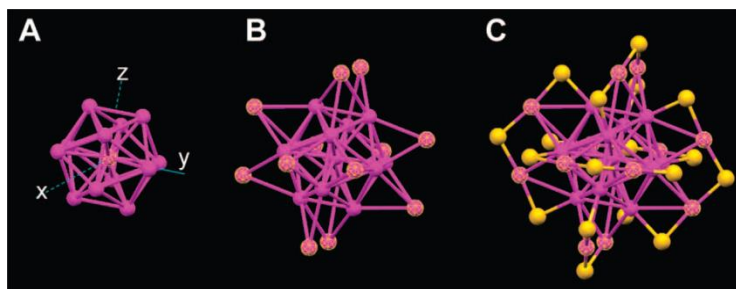


Figure 1.9: Crystal structure of $\text{Au}_{25}(\text{SR})_{18}$ cluster. A) the icosahedral Au_{13} core, B) the Au_{13} core plus the exterior 12 Au atoms, C) the whole Au_{25} cluster protected by 18 thiolate ligands (only S shown in yellow). Reproduced from Ref. 31.

$\text{Au}_{25}(\text{SR})_{18}$

Perhaps the most extensively studied system, the $\text{Au}_{25}(\text{SR})_{18}$ provides an excellent model for a understanding of the detailed cluster structure–property relationships based upon experiment and theory (Figure 1.9). In figure 1.10 the absorption spectrum of $\text{Au}_{25}(\text{SR})_{18}$ shows multiple bands at 670 nm, 450 nm, and 400 nm. The calculated spectrum of $\text{Au}_{25}(\text{SR})_{18}$ agrees well with the experimental one. The electronic transition at $\lambda = 670$ nm corresponds to the LUMO \leftarrow HOMO transition (Figure 1.11), which is essentially an intraband (sp \leftarrow sp) transition.

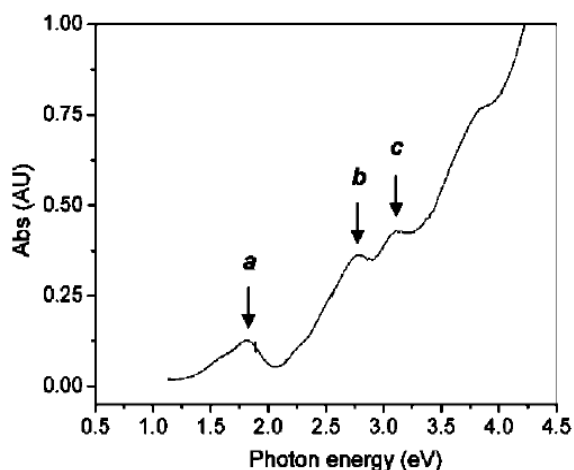


Figure 1.10: UV-Vis spectrum of Au_{25} clusters. Reproduced from Ref. 31.

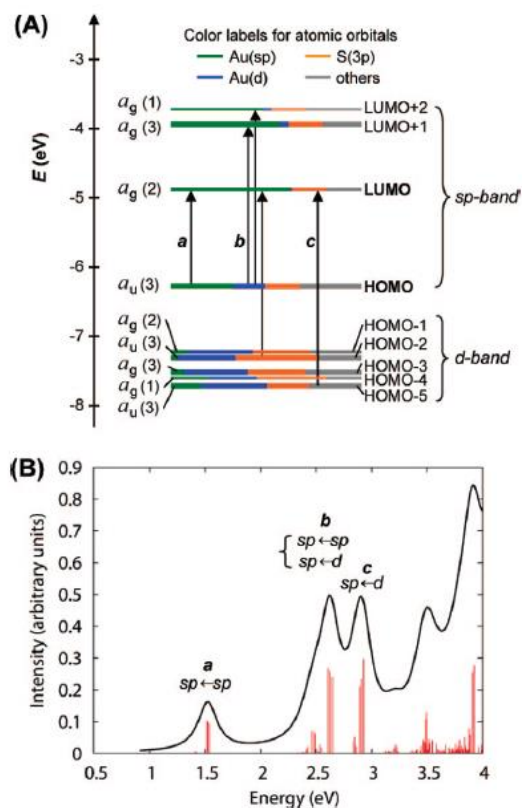


Figure 1.11: (A) Kohn–Sham orbital energy level diagram for a model compound $\text{Au}_{25}(\text{SH})_{18}$. Each KS orbital is drawn to indicate the relative contributions (line length with color labels) of the atomic orbitals of Au (6sp) in green, Au (5d) in blue, S (3p) in orange, and others in gray (those unspecified atomic orbitals, each with a $< 1\%$ contribution). The left column of the KS orbitals shows the orbital symmetry (g, u) and degeneracy (in parentheses); the right column shows the HOMO and LUMO sets. (B) The theoretical absorption spectrum of $\text{Au}_{25}(\text{SH})_{18}$. Peak assignments: peak (a) corresponds to 1.8 eV (observed), peak (b) corresponds to 2.75 eV (observed), and peak (c) corresponds to 3.1 eV (observed). Reproduced from Ref. 31.

The band at 450 nm (peak b) comes from the mixed intraband ($sp \leftarrow sp$) and interband ($sp \leftarrow d$) transitions. The transition at 400 nm (peak c) mainly arises from the interband ($sp \leftarrow d$) transition. Overall, the molecule-like multiple absorption bands of $Au_{25}(SR)_{18}$ nanoclusters are all due to single-electron transitions between quantized electronic energy levels²⁸.

For thiolate-capped gold clusters, Negishi et al. reported an observation of paramagnetism in $Au_n(SG)_m$ clusters but the origin of magnetism was not completely understood due to the unavailable crystal structures of these clusters²⁹. In recent work, paramagnetism was observed in charge neutral $[Au_{25}(SR)_{18}]^0$ clusters³¹. It has been shown that the magnetism in the cluster can be

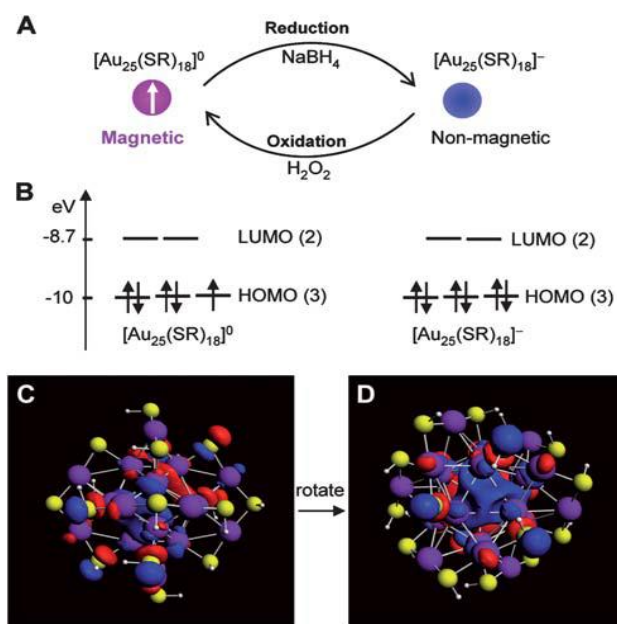


Figure 1.12: (A) Reversible conversion between the neutral and anionic $Au_{25}(SR)_{18}$ nanoclusters. (B) DFT calculated Kohn–Sham orbital level diagram for the neutral and anionic nanoclusters, respectively. (C–D) Views of the highest occupied Kohn–Sham orbital for $[Au_{25}(SH)_{18}]^0$ at the LB94//Xa/TZP level of theory. The HOMO possesses two lobes and exhibits distinct P-like character. (D) is rotated relative to (C) to show one of the lobes (contributed by three Au atoms in the icosahedral shell). (Purple: Au, yellow: S, white: H atoms). Reproduced from Ref. 31.

reversibly switched on or off by controlling the charge state of the $[\text{Au}_{25}(\text{SR})_{18}]^q$ cluster, that is, the anionic cluster is non-magnetic while the neutral one is magnetic (Figure 1.12). With the crystal structure of $[\text{Au}_{25}(\text{SR})_{18}]^0$, a correlation of crystal structure and magnetic properties has been achieved. DFT calculations based on the crystal structure of $[\text{Au}_{25}(\text{SR})_{18}]^0$ successfully explained the origin of the magnetism. It is found that the unpaired spin in the $[\text{Au}_{25}(\text{SR})_{18}]^0$ cluster arises from the highest occupied Kohn–Sham orbital³⁰. The results of this study demonstrate the versatility of the $\text{Au}_{25}(\text{SR})_{18}$ cluster and a possible application as a paramagnetic probe.³¹

1.6 Phosphine protected clusters

In addition to thiols, phosphine molecules have been used as protecting ligands in the synthesis of metal clusters. This is due to the intriguing properties of phosphine-stabilized metal clusters.

Au₅₅

In 1981, Schmid et al. synthesized $\text{Au}_{55}(\text{PPh}_3)_{12}\text{Cl}_6$ nanoclusters with an average core size of 1.4 ± 0.4 nm. Diborane gas was used as the reducing agent under anaerobic conditions in the preparation. This was deemed too complicated a synthetic route to be a popular method for preparation of phosphine-ligated metal nanoclusters³². Hutchison and co-workers developed a safer, more convenient, and more versatile synthesis of phosphine-ligated gold clusters. The advantages of their method is: (1) eliminating the use of diborane or borane; (2) the synthesis process could be carried out under ambient conditions; (3) a variety of phosphines as passivating ligands are permitted; (4) allowing for control over cluster core size³³.

Additionally, $\text{Au}_{55}(\text{PPh}_3)_{12}\text{Cl}_6$ clusters on gold substrates have been investigated by bringing individual particles into contact with an STM tip. From this, I - V data reveals that these

particles exhibit well-expressed Coulomb blockades at room temperature, Figure 1.13³⁴. This opens up future applications in nanoelectronics. The same Au_{55} species has been studied by the same technique, at 7 K under ultra-high vacuum (UHV)³⁵. Figure 1.14 shows an STM image of the Au_{55} core cluster³.

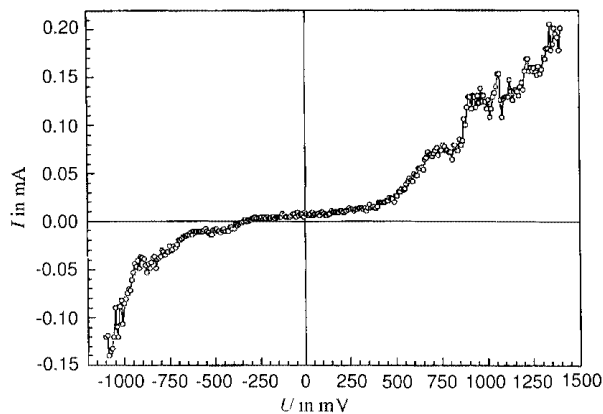


Figure 1.13: Room temperature IV characteristics of an individual $\text{Au}_{55}(\text{PPh}_3)_{12}\text{Cl}_6$ cluster indicating a well-expressed Coulomb blockade. Reproduced from Ref. 35.

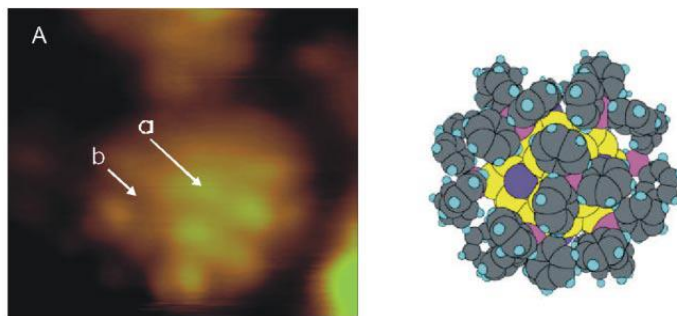


Figure 1.14: STM image of an individual $\text{Au}_{55}(\text{PPh}_3)_{12}\text{Cl}_6$ cluster at 7 K under UHV conditions together with a full-space model; the light dots indicate phenyl rings; the positions **a** and **b** indicate where the measurements have been performed to yield the IV characteristics. Reproduced from Ref. 35.

Au₂₀

Wang et.al. report the synthesis and structure of a new Au₂₀ nanocluster coordinated by four tripodal tetraphosphine (PP₃) ligands. This method involves first synthesizing a Au₄Cl₄PP₃ complex, which is then dissolved in a heated dichloromethane solution. The addition of NaBH₄ in ethanol is then quickly added and mixture is stirred. After removal of the solvent, the dark red residue was washed by a toluene/dichloromethane solution until the color of the wash solution changed, at which the left residues were dissolved in a dichloromethane/toluene solution, which became red. Red crystals were grown by evaporation of the dichloromethane/toluene. Single-crystal X-ray crystallography and electrospray ionization mass spectrometry show that the cluster assembly is [Au₂₀(PP₃)₄]Cl₄. The Au₂₀ cluster consists of an icosahedral Au₁₃ core and a seven-Au-atom partial outer shell arranged in a local C₃ symmetry (figure 1.15). One PP₃ ligand coordinates to four Au atoms in the outer shell, while the other three PP₃ ligands coordinate to one Au atom from the outer shell and three Au atoms from the surface of the Au₁₃ core, giving rise to an overall chiral 16- electron Au cluster core with C₃ symmetry³⁶. This work improves on

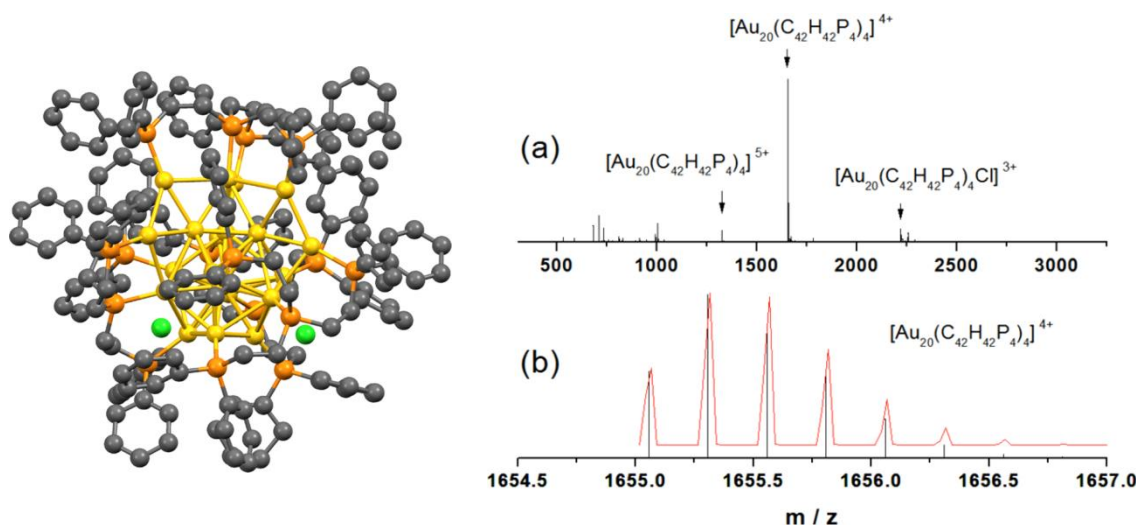


Figure 1.15: [Au₂₀(PP₃)₄]Cl₄ structure (left) , Mass spec indicating formation of monodisperse Au₂₀ (right). Reproduced from Ref. 36.

a previously reported photoelectron spectroscopy study of a gas phase synthesis of a Au_{20} cluster³⁷. Additionally, Wang *et al.* reported synthesis of a $\text{Au}_{22}(\text{L}^8)_6$ cluster [$\text{L}^8 = 1,8$ -bis(diphenylphosphino)octane], where the Au core consists of two Au_{11} units and contains eight uncoordinated surface Au atoms. The eight uncoordinated surface Au atoms in the $\text{Au}_{22}(\text{L}_8)_6$ nanocluster are unprecedented in atom-precise Au nanoparticles and can be considered as potential in situ active sites for catalysis³⁸. (Figure 1.15)

Au_n (n=7–12)

Phosphine-capped gold clusters are commonly prepared by the use of sodium borohydride to reduce triarylphosphine and triphenylphosphine gold complexes. Vandervelden *et al.* successfully prepared $[\text{Au}_7(\text{PPh}_3)_7]^+$ and $[\text{Au}_8(\text{PPh}_3)_6\text{I}]\text{PF}_6$ clusters³⁹. Recently, Zhang *et al.* reported the synthesis of PPh_3 -protected tetrahedral Au_{20} clusters coordinated with eight PPh_3 ligands by using a similar two-phase system to that used for the synthesis of small phosphine- and thiol-stabilized gold clusters³⁶.

Diphosphine ligands have a great propensity for synthesizing phosphine-protected gold clusters with a narrow size distribution^{40,41}. For example, Bertino and co-workers proposed a new synthetic strategy for synthesizing monodisperse gold nanoclusters by using diphosphine ligands^{32,42}. They report a monophasic and single pot synthesis using a bidentate phosphine ligand, $\text{P}(\text{Ph})_2(\text{CH}_2)_M\text{P}(\text{Ph})_2$, and triphenyl phosphine gold (I) chloride, $\text{Au}(\text{PPh}_3)\text{Cl}$, precursor dissolved in an organic solvent. The Au(I) is reduced slowly by borane-tert-butylamine complex (BTBC) to form Au clusters coordinated by the diphosphine ligand. The Au clusters were characterized by high-resolution mass spectrometry and UV-vis absorption spectroscopy. The mean cluster size obtained depends on the chain length M of the ligand. Single monodispersed Au_{11} (Figure 1.16)

is obtained with the $\text{P(Ph)}_2(\text{CH}_2)_3\text{P(Ph)}_2$ ligand, whereas $\text{P(Ph)}_2(\text{CH}_2)_M\text{P(Ph)}_2$ ligands with $M = 5$ and 6 yield Au_{10} and Au_8 clusters. Their work suggests that diphosphines provide a set of flexible ligands to allow size-controlled synthesis of Au nanoparticles⁴². Hong et. al. utilized scalar relativistic density functional theory (DFT) calculations using the projector augmented wave scheme (PAW) to examine reactivity and selectivity of diphosphine ligands of the form $\text{P(Ph)}_2(\text{CH}_2)_M\text{P(Ph)}_2$ with $M = 3, 5$ and 10 toward small Au_n ($n = 7-11$) clusters. Calculations suggest that flexibility and reactivity of spacer plays a key role in size selectivity⁸.

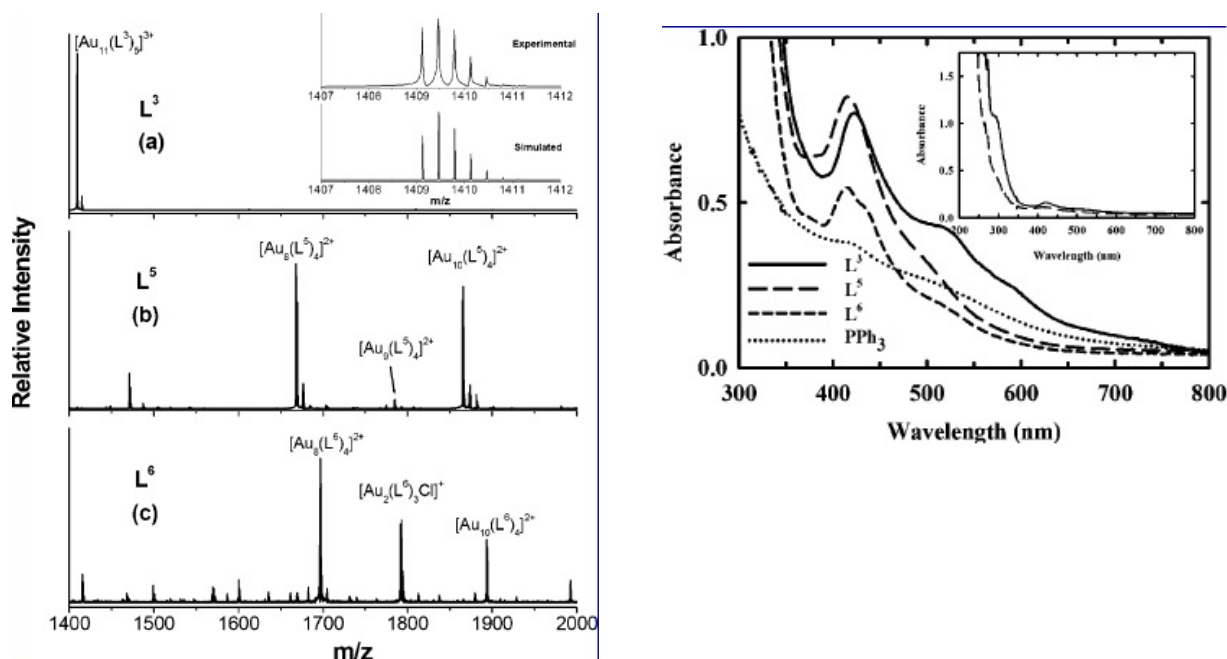


Figure 1.16: Mass spec of L^3 , L^5 and L^6 ligated Au clusters (left), UV-Vis comparison of the same ligands (right). Reproduced from Ref. 42.

1.7 Nanopores and Sensing

The Coulter counter, which is a device that measures resistive pulses to detect microscopic particles $\sim 10\ \mu\text{m}$ -size particles, was the basis behind the development and use of biological channels, i.e. α -hemolysin (α -HL) (fig. 1.17 left), as a sensing element.⁴³ A coulter counter is an apparatus used to count and size particles suspended in an electrolyte. It usually contains two chambers separated by a membrane containing a fixed size opening, which allows current to flow. It based on the Coulter principle that states that the measurable changes in impedance produced by particles passing through the opening is proportional to the volume of the particle.

In our nanopore, the α -HL can be embedded into a planar lipid bilayer and the single channel element is used to detect individual analyte/channel interactions that can be interpreted to give information about the analyte identity and concentration. This is achieved by measuring the variations in the ionic current generated by analytes flowing into or through a nanopore^{43,44}. When an analyte enters the pore we see a reduction in the ionic current indicating a “blocked state” (fig. 1.17 center). The reaction kinetics are characteristic of the chemical interactions between the analyte and the pore and can tell us information about the type of analyte based off the dynamics

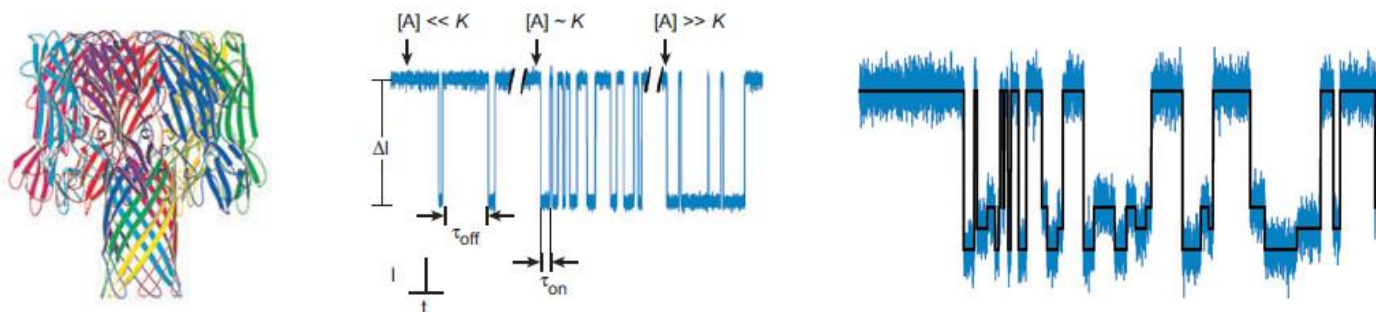


Figure 1.17: (left) α -hemolysin nanopore, (center) ionic current blockades, (right) multistate current blockades. Reproduced from ref 43.

of the current fluctuations⁴³. Figure 1.17 (right) shows a multistate ionic current that can come out of the analyte/pore interaction which could indicate important information regarding the conductance states of the analyte.

The size of the analyte that can be detected is limited to the opening of the nanopore (~ 2 nm for α -HL). Typically, nanopore sensing has been used primarily in the detection of metal ions, proteins, peptides, DNA, etc.

1.8 Nucleation of Clusters

The process of nucleation of metal nanoclusters has been extensively studied for many years. However, it is difficult to describe exactly how nucleation and growth of nanoparticles occur due to the complicated kinetics and mechanistics of the system. This is due primarily to the number of variables that are present in the synthesis. For example, the role of ligands in transition metal nanoparticle synthesis is not clearly understood. Ligands do exhibit the ability to control growth and size distribution of the nanocluster formation leading to very stable end-products, however, questions about how they interact and control growth still exist. Questions such as, “are they involved in every step of the formation of nanoclusters?”, “or do they bind to nanoclusters after the metal core is formed?”, are still being considered⁴⁵. As stated earlier, much work has been done that shows the formation of stable Au-NP's in aqueous solutions via reduction with ligands. In this review, I will present a general overview of the theory for the synthesis of the gold clusters discussed in the paper. Typically, the process is described in terms of Ostwald's rule of stages, Ostwald ripening and the LaMer crystallization model⁴⁶.

Friedrich Wilhem Ostwald (1853-1932) noticed that the transformation of unstable states into stable states usually happened in stages, with the first products being intermediate products

having free energies close to the initial states. Also important to the metastability condition is the contribution of the interfacial free energy to the total energy of the system, wherein the contribution is significant for nanoclusters. Ostwald ripening is when most small clusters formed initially in the system dissolve at the expense of growing larger clusters. It is caused by the change in solubility of the nanoclusters as described by the Gibbs-Thomson equation:

$$C_r = C_\infty \exp\left(\frac{2\gamma\Omega}{rRT}\right)$$

with: C_r the solubility of a spherical particle with radius r at its surface, C_∞ the solute concentration, γ the specific interfacial energy of the solution-particle boundary, Ω the mean atomic volume of a particle, R the ideal gas constant, and T the absolute temperature. For smaller particles, the increase in solubility and larger surface energy leads to it dissolving.

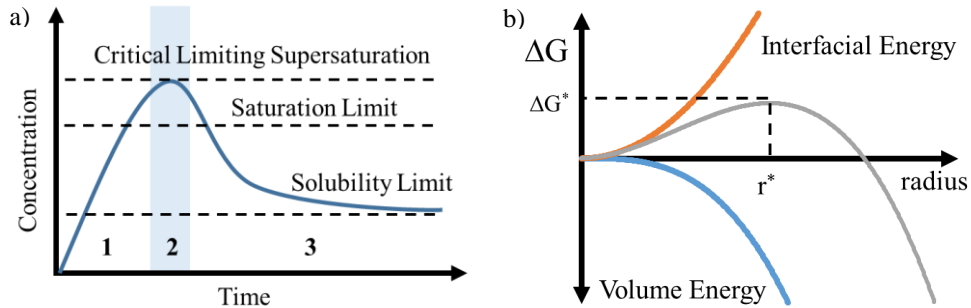


Figure 1.18: a) LaMer's mechanism describing the nucleation process: 1. rapid increase in molecular concentration, 2. the formation of stable clusters, 3. decrease in molecular material due to nucleation. b) Graph of cluster free energy vs. cluster radius according to classical nucleation theory. The critical radius r^* and critical activation energy ΔG^* for stable clusters are shown.

LaMer's model for crystallization was the next step in understanding growth of crystal sols and consisted of three stages (Figure 1.18a). The first step involved the rapid increase in molecular materials until a critical concentration is reached (step 1 and 2 in figure 1.18a). The critical concentration or supersaturation limit is described by:

$$\frac{\Delta\mu}{k_B T} = \ln \frac{C}{C_s}$$

with k_B the Boltzman constant and T the temperature. From this point, clusters begin to be stable enough for nucleation to begin. This point (step 2) is often referred to “burst nucleation” or “LaMer burst”^{45,47,48}. A decrease in the free energy (ΔG) accompanies the formation of stable clusters and is described by:

$$\Delta G = -\frac{V}{\Omega} k_B T \ln \beta + S\gamma$$

where $\beta = C/C_s$ and V and S are the volume and surface area of the cluster and illustrated in figure 1.18b. Considering a spherical particle the above equation becomes:

$$\Delta G = -\frac{4\pi r^3}{3\Omega} k_B T \ln \beta + 4\pi r^2 \gamma .$$

Using this equation we can derive the conditions for the critical radius (r^*) and critical activation energy (ΔG^*) for which growth is favored:

$$r^* = \frac{2\Omega\gamma}{k_B T \ln \beta} \quad \text{and} \quad \Delta G^* = \frac{1}{3} (4\pi r^{*2} \gamma) .$$

We can see that the activation energy required for the formation of a stable cluster, at supersaturation β , is 1/3 the energy required to create its surface. We can also see that nucleation is a competition between coalescing and re-dissolution of clusters in solution⁴⁶. The nucleation rate can also be determined using the kinetic factor and the activation energy and is given as:

$$J = K_0 \exp\left(\frac{-\Delta G^*}{k_B T}\right)$$

with $K_0 = N_0 v_0$ and N_0 the solubility of the materials and v_0 the frequency at which critical nuclei become supersaturated and form crystals.

After, molecular concentration begins to decrease (step 3) due to the formation of clusters, thus relieving the supersaturation. Nucleation in step 3 can occur in two ways, either homogeneous or heterogeneous nucleation. Once the concentration is below the supersaturation limit, nucleation no longer occurs and growth can continue through Ostwald ripening and diffusion kinetics. The clusters will continue to grow until the concentration drops below the solubility limit where the cluster will reach equilibrium. This links back into the beginning of this section and the role of ligands. My work focuses on the use of thiol or phosphine based ligands to inhibit growth of these clusters, limiting them to a fixed number of Au atoms comprising the core of the cluster.

CHAPTER 2: Experimental Analytical Techniques

2 Experimental Analytical Techniques

2.1 Electrospray Ionization Mass Spectrometry (ESI-MS)

Electrospray Ionization Mass Spectrometry is a powerful analytic technique used in all areas of science for the analysis of molecules. ESI-MS is a soft ionization technique that can measure large and small molecules operating at atmospheric pressure and moderate temperatures^{49–51}. The process of ESI can be divided into three steps:

1. The production of charged droplets at the electrospray capillary tip
2. The reduction of the size of the charged droplets by solvent evaporation and charge induced disintegrations
3. The mechanism leading to the production of gas phase ions from the droplets.

These steps occur at atmospheric pressure in the first stage to the apparatus (figure 2.1a), before entering the vacuum region of the mass spec device (figure 2.1b).

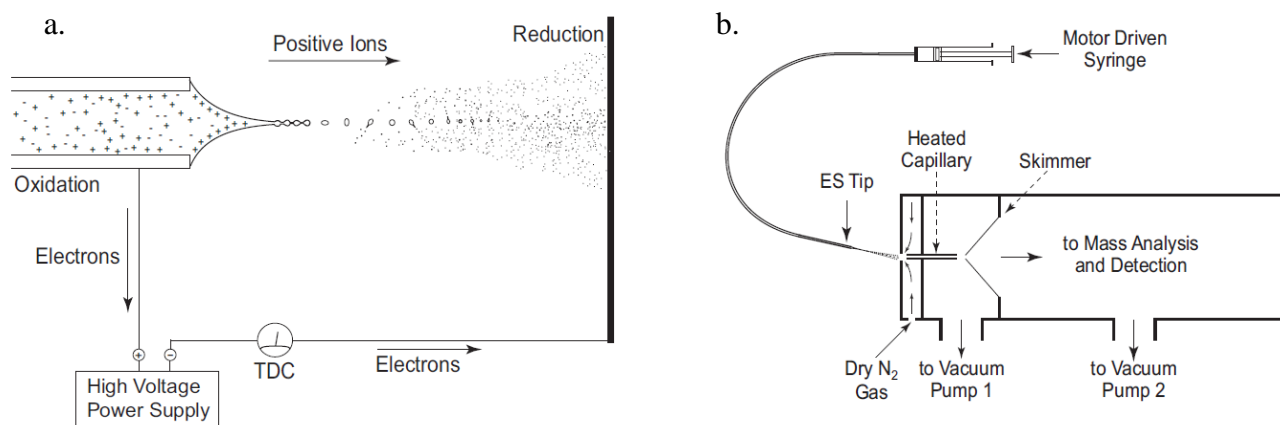


Figure 2.1: a. Picture of the 3 major steps of ESI in the atmospheric pressure region run in positive ion mode. b. Picture of an electrospray ion source and mass spectrometer. Sample is inserted via the syringe. Reproduced from Ref. 51.

A voltage, V_c , of up to a few kV is applied to the spray capillary which is located a few centimeters from the counter electrode. The electric field produced at the capillary tip can be estimated by the following relationship:

$$E_c = \frac{2V_c}{r_c \ln(4d / r_c)}$$

where V_c = capillary voltage, r_c = outer radius of the capillary, and d = distance from capillary to counterelectrode.

Due to the very small tip and high voltage, the electric field at the tip is very high ($E_c \approx 10^6$ V/m) and results in the polarization of the solvent near the tip. In positive mode, this leads to an increase in the number of positive ions at the surface of the meniscus and negative ions moving away and yields the formation of a cone, known as a Taylor cone.^{51,52} When the applied field is strong enough, a fine jet emerges from the cone, where the surface of the jet is charged positively. As the solvent evaporates and the charge remains constant the droplet size begins to decrease. At a certain radius the electrostatic repulsion between the charges overcomes the surface tension at the droplet surface leading to what is known as coulomb fission (or coulomb explosion). This process is illustrated in Figure 2.2 below.

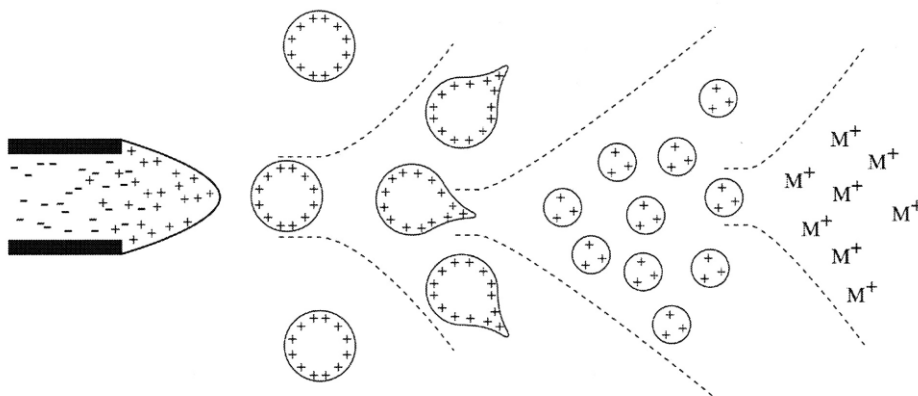


Figure 2.2: The mechanism for electrospray ionization. Reproduced from Ref. 50.

Evaporation of the solvent is caused by the thermal energy of the ambient gas, which is usually air at atmospheric pressure. Again, as the droplet size gets smaller, the repulsive force overcomes the cohesive force resulting in an instability of the droplet. The condition for this instability or coulomb fission is given by the Raleigh equation:

$$Q_{Ry} = 8\pi(\epsilon_0\gamma R^3)^{1/2}$$

where Q_{Ry} is the charge on the droplet, γ the surface tension of the solvent, R is the radius of the droplet and ϵ_0 is the permittivity.⁵³

Once the nanoclusters are ionized, they pass into the mass spectrometer sections of the instrument. The ESI-MS used in the analysis of the clusters in this paper makes use of the linear ion trap mass quadrupole spectrometer. Mass spectrometry measures the mass-to-charge ratio of ions to identify, quantify and provide structural and chemical information of known and unknown compounds. The mass spectrometer has a series of quadrupole mass filters that allow ions of a specific mass-to-charge (m/z) ratio to pass through to the detector. DC and RF drive voltages are applied to the various quadrupoles sections independently or in combination to move or trap ions. The motion of ions in a quadrupolar field (please note that the term “quadrupolar” in this description refers to the fact that the potential within the device depends on the square of the distance from the origin) are described by the solutions to the second-order linear differential equation first introduced by Mathieu in 1868.

Starting with an expression for the potential in rectangular coordinates for a quadrupole device:

$$\phi_{x,y,z} = A(\lambda x^2 + \sigma y^2 + \gamma z^2) + C,$$

where λ , σ , γ are weighting constants for the x , y , and z coordinates, A refers to the potential applied between the opposite polarity electrodes and C is a fixed potential. In addition, we can treat the

components of the ion motion in the field to be independent of each other. In an electric field, the Laplace condition must be satisfied, therefore:

$$\nabla^2 \phi_{x,y,z} = A(2\lambda + 2\sigma + 2\gamma) = 0$$

we then obtain:

$$\lambda + \sigma + \gamma = 0.$$

For the 2-D Quadrupole Mass Filter (QMF) and the Linear Ion Trap (LIT), the weighting constants have been found to be:

$$\lambda = -\sigma = 1 \quad \gamma = 0$$

Substituting these values into the above equation yields:

$$\phi_{x,y} = A(x^2 - y^2) + C$$

The QMF consists of circular rods, where each pair of opposite rods are connected electrically establishing a 2-D quadrupole field in the x - y plane (Figure 2.3). When potentials are applied to the rods, ions traveling along the z -direction can begin to oscillate in the x - y plane. These oscillations are a property of the mass-to-charge ratio (m/z) for the ion, and, with suitable electrical conditions, ions of a specific m/z will be able to make the entire length of the quadrupole. The quadrupole potential is given by the difference between the x pair and y pair electrodes:

$$\phi_0 = \phi_{x \text{ pair}} - \phi_{y \text{ pair}}$$

Under the conditions when $y = 0$, $x^2 = r_0^2$, the equation above becomes:

$$\phi_{x \text{ pair}} = A(r_0^2) + C \text{ and likewise, } \phi_{y \text{ pair}} = A(-r_0^2) + C$$

and we find:

$$\begin{aligned} \phi_0 &= 2Ar_0^2 \\ \therefore A &= \frac{\phi_0}{2r_0^2} \end{aligned}$$

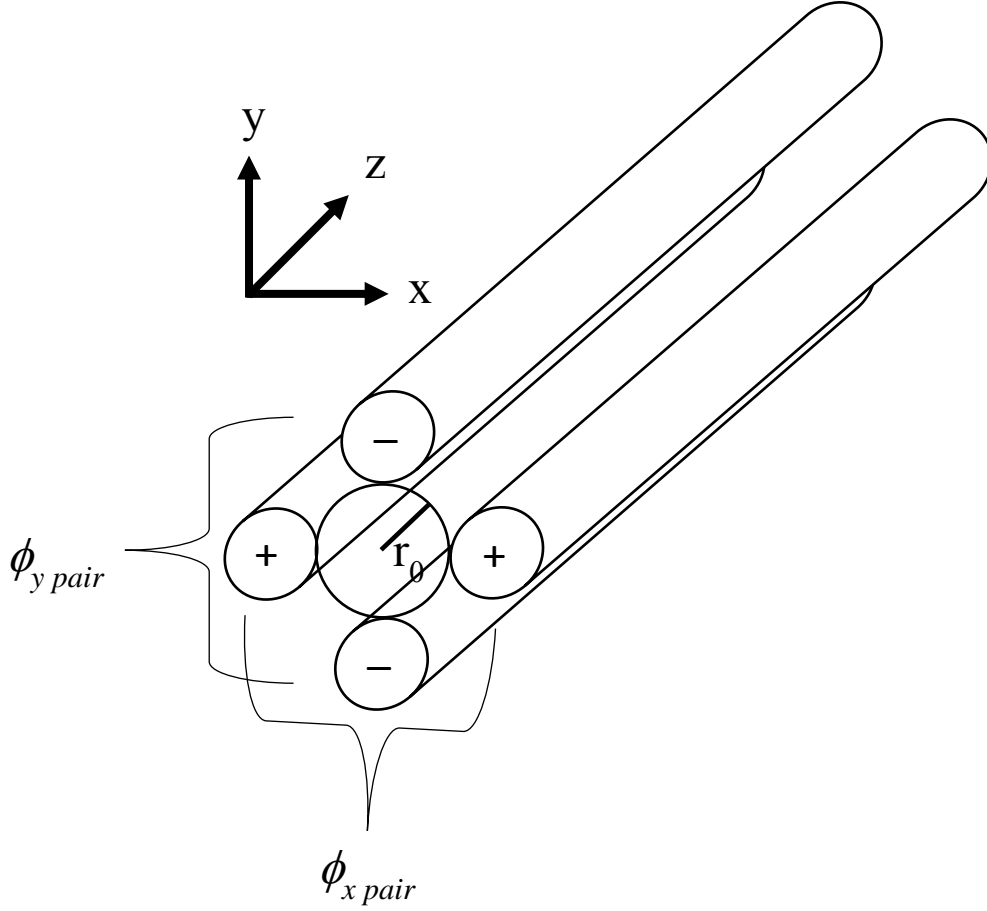


Figure 2.3: Picture of the quadrupole device (QMF).

So, at the origin ($x = 0$, $y = 0$) and zero ground potential ($C = 0$) the potential becomes:

$$\phi_{x,y} = \frac{\phi_0}{2r_0^2} (x^2 - y^2)$$

We can calculate the electric field at the point (x , 0) by the derivative of the potential with respect to x , and then determine the force on an ion in the x – direction by:

$$F_x = -e \left(\frac{d\phi}{dx} \right)_y = -e \frac{\phi_0 x}{r_0^2}$$

Now, if we consider a real system with:

$$\phi_0 = 2(U + V \cos \Omega t) \text{ with } U - \text{DC potential, } V - \text{amplitude of RF potential.}$$

and applying Newton's second law to obtain a second-order differential equation:

$$F_x = m \left(\frac{d^2 x}{dt^2} \right) = -e \frac{\phi_0 x}{r_0^2}.$$

We can then use the solution to the Mathieu equation (given in its common form):

$$\frac{d^2 u}{d\xi^2} + (a_u - 2q_u \cos 2\xi)u = 0$$

where u is the displacement and ξ is a dimensionless parameter equaling $\Omega t/2$, with Ω being the frequency, t is the time, and a_u and q_u are the trapping parameters, to determine the trapping parameter relationships for the x and y displacements for a 2-D QMF or LIT. The relationships are given as follows:

$$a_x = \frac{8eU}{mr_0^2\Omega^2} \text{ and } q_x = \frac{-4eV}{mr_0^2\Omega^2}$$

When repeating the derivation for the y direction we get the relationship: $a_x = -a_y$ and $q_x = -q_y$, which is obtained from $\lambda = -\sigma = 1$ from earlier. As we can see, the trapping parameters are functions of the DC or RF voltage, the RF frequency, mass/charge ratio and size of the device, all of which are instrumental parameters that control the operation of the QMF.

2.2 Ultraviolet – Visible Spectroscopy

Ultraviolet – Visible spectroscopy is another powerful technique that can give a wealth of information about a sample. It is a quick simple test that is commonly used in many analytical chemistry labs for the quantitative determination of different analytes. The principles behind UV-Visible are based on the absorption of wavelengths of light by a sample and is the complementary to fluorescence. Incident light on a sample can have sufficient energy to excite an electron from the ground state to a higher energy orbital. The following electronic transitions that are possible are:

$n \rightarrow \pi^*$, $\pi \rightarrow \pi^*$, $n \rightarrow \sigma^*$, $\pi \rightarrow \sigma^*$, $\sigma \rightarrow \pi^*$, $\sigma \rightarrow \sigma^*$ (shown below)

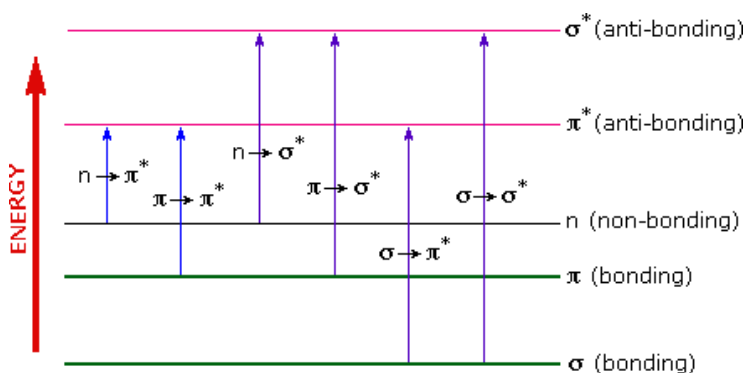


Figure 2.4: Possible electron transistions. Reproduced from chemistry.msu.edu

In each case, the electron can be excited from a full orbital to an empty anti-bonding orbital. Of the 6 transitions shown, only the $n \rightarrow \pi^*$, $\pi \rightarrow \pi^*$ (blue) fall in the UV-Visible region of the spectrum.

When utilizing ultraviolet-visible spectroscopy for the analysis of metal nanoparticles, we typically look at excitation of the particles in terms of the localized surface plasmon resonance (LSPR). Surface plasmon resonance is a coherent oscillation of the surface conduction electrons excited by electromagnetic radiation. The LSPR wavelength of metal NP's is strongly

dependent on the size, shape, inter-particle distance, type of metal and the dielectric constant.

The plasma frequency is given by:

$$\omega_p = \sqrt{\frac{n_e e^2}{m \epsilon_0}}$$

For nanoparticles where $d \ll \lambda_{\text{light}}$ the polarizability is defined as:

$$\alpha = 3\epsilon_0 V \left(\frac{\epsilon - \epsilon_m}{\epsilon + 2\epsilon_m} \right)$$

where V – volume, ϵ_0 – permittivity of free space, ϵ - dielectric function of the metal [$\epsilon = \epsilon_r + i\epsilon_i$]

and ϵ_m – dielectric constant of the surrounding medium.

With a nanoparticle extinction cross-section (C_{ext}):

$$C_{\text{ext}} = \frac{24\pi^2 R^3 \epsilon_m^{3/2}}{\lambda} \frac{\epsilon_i}{(\epsilon_r + 2\epsilon_m)^2 + \epsilon_i^2}$$

2.3 *Transmission Electron Microscopy*

The invention of the electron microscope in 1931 by Ruska and Knoll, revolutionized the way we see materials. The first commercial Transmission Electron Microscopes (TEM) were developed a few years later, beginning in 1936. TEM is performed in high vacuum and typically consists of an electron gun, a system of condenser lens and an imaging system. Electrons generated by thermionic emission from the gun are accelerated through a high voltage and pass through the condensing lenses (magnetic lenses) where they can be focused onto the specimen and transmitted through to a phosphorescent screen or a CCD camera.

A key benefit of using electrons is that they overcome the image resolution limitations of optical microscopes, which is based on the wavelength of visible light. Where the resolution of an electron microscope is based on the wavelike properties of the electron proposed by Louis de Broglie in 1925 and can be determined by:

$$\delta \approx \frac{1.22\lambda}{\beta}$$

where λ is the wavelength of the electron, and β is the semi-angle⁵⁴.

Starting with the de Broglie equation relating a particles momentum to its wavelength:

$$\lambda = \frac{h}{p}$$

The accelerating electron in the TEM gains kinetic energy as it moves through a potential V .

Based on conservation of energy the kinetic energy equals the potential energy, so:

$$eV = \frac{m_0 v^2}{2}$$

From the momentum of the electron we get:

$$p = m_0 v = (2m_0 eV)^{1/2}$$

By combining the three above equations, we can get an expression for the electron wavelength in terms of the electric potential:

$$\lambda = \frac{h}{(2m_0eV)^{1/2}}$$

Interestingly, for electrons accelerated by energies > 100 keV (typical range for commercial TEMs) reach velocities greater than half the speed of light and therefore relativistic effects should be taken into consideration. We can derive a new relationship between electron accelerating potential and wavelength with relativistic effects as:

$$\lambda = \frac{h}{\left[2m_0eV \left(1 + \frac{eV}{2m_0c^2} \right) \right]^{1/2}}$$

For a TEM with a 100 keV electron, $\lambda \sim 4$ pm, which is much smaller than light, and as can be seen in the above equations, as electron energy increases, electron wavelength decreases, and therefore so does resolution⁵⁴.

A major limitation to the TEM is that samples need to be thin, or electron transparent. In other words, the sample needs to be thin enough to transmit a sufficient amount of electrons to the screen. The thickness of a sample does depend on the material being studied and the information the user would like to get from the beam. A TEM can also take advantage of the other information that the interactions of the high-energy electrons incident on the sample give. These secondary benefits include electron diffraction from a crystal, and electron energy loss spectroscopy (EELS), which measures the energy lost by inelastically scattered electrons and can be used to determine chemical composition. The wealth of data that a transmission electron microscope can acquire makes it an invaluable tool for research.

2.4 X-Ray Techniques

X-Ray Diffraction (XRD) is a very popular and relatively simple method used in determining the crystal structure of materials that exhibit long range ordering. It can be performed at atmosphere and can be measure both bulk and nanomaterial in the solid or liquid phase. XRD is an elastic scattering process in which X-rays are scattered by the electrons distributed around atoms. The wavelength and energy remains constant throughout the process while the momentum or wavevector (k) changes. By conservation of momentum we get:

$$k_0 = k' + g$$

where k_0 and k' are the initial and scattered wavevector and g represents the change in momentum. It is important to note that $|k_0| = |k'|$, in other words, there is only a change in direction of the beam not the magnitude.

The theory of XRD is based on the principle of wave interference. For materials with periodic lattice spacing d , the distance between planes is determined by the constructive interference pattern produced by the scattered X-rays. Constructive interference of waves is obtained for angles that satisfy the condition:

$$2d \sin \theta = n\lambda$$

known as the Bragg condition. Information about the lattice crystal size and symmetry can be obtained from the position of the diffracted beams.

X-Ray Photoemission Spectroscopy (XPS) is another powerful X-ray technique that is useful in determining the elemental composition of a sample. It is often referred to as Electron Spectroscopy for Chemical Analysis or ESCA. XPS gives information about the empirical formula, chemical state and electronic state of the elements that comprise a material. The theory of XPS is based on Einstein's photoelectric effect where incident radiation on a surface with

sufficient energy will eject an electron. The energy of the ejected electron can be measured by the Einstein equation:

$$E_B = h\nu - KE$$

where E_B is the binding energy of the electron in the atom, $h\nu$ is the energy of the X-Ray source and KE is the kinetic energy of the emitted electron. The energy of the X-Ray source is a known value, and the kinetic energy of the ejected electron is measured in the spectrometer. From this information, the binding energy of the electron to the atom is determined, which is a function of the atom and is used to determine what the material is.

**CHAPTER 3 Synthesis of gold clusters with flexible and rigid
diphosphine ligands and the effect of spacer and solvent on the size
selectivity**

3 Synthesis of gold clusters with flexible and rigid diphosphine ligands and the effect of spacer and solvent on the size selectivity

3.1 Introduction

Synthetic developments of monodisperse monolayer protected clusters (MPC's) are rapidly becoming an exciting area of research^{9,55,56}. Gold nanoclusters exhibit optical properties that make them candidates for applications such as data storage, ultrafast switching and gas sensors⁸. Additionally, gold nanoclusters have the potential to be utilized in drug delivery systems, cancer therapy and treatment for Alzheimers disease, and for their use in catalysis^{9,11,12,57,58}. Most current synthetic techniques however typically produce polydisperse suspensions. Monodispersity can be obtained only with difficulty and it often requires additional processing steps, such as crystallization or separation (e.g. chromatography)^{59,60}. Phosphine based ligands are commonly used to form metal complexes and have shown to be an efficient, size selective capping agent, including a significant body of literature utilizing triphenylphosphine (PPh₃). However, diphosphines have recently gained considerable attention as capping agents, due to their size selectivity, and simplified processing^{8,38,42,61}.

A synthetic pathway to attain size selective, ultra-small Au MPC's with diphosphine ligands PPh₂(CH₂)_MPPh₂ in a single phase one pot scheme was achieved previously by our group⁴². This method involves the dissolving of Chloro(triphenylphosphine)gold(I) (Au(PPh₃)Cl) and a diphosphine ligand in an organic solvent with the addition of borane-*tert*-butylamine (BTBC) as the reducing agent. The effect of varying the aliphatic bridge length M on size selectivity of the MPCs has been studied for the M = 3, 5, 6 and 10

ligands^{8,41,62}. The flexibility of spacer and the strength of the ligand-gold interaction are responsible for this selectivity. For example, the largest selectivity was achieved with the shortest spacer, $M = 3$, and as the length or flexibility of spacer group was increased, the selectivity decreased. This indicates that the more flexible ligands can adopt new geometries that can increase bond strength between the Au and ligand, resulting in the size-selecting control of L^3 toward small gold clusters. The reaction network for L^3 and L^5 ligands was proposed by Hudgens *et al.*^{61,63}. This work showed that alkyldiphosphines are ideal ligands for studying the effect of chain length and flexibility on size selectivity, but the conditions that are responsible for the selectivity are much more complex than just using different chain lengths of the alkyl spacer⁶⁴.

Another ligand relevant to this work is PPh_3 . This ligand is commonly used in the formation of closed shell metal clusters and has been shown to be an effective etching agent⁶⁵. However, PPh_3 is not a size selective ligand and it yields polydisperse suspensions^{42,64,66,67}. This lack of selectivity is due to the kinetics of the reaction, which can be manipulated based on reduction rates and trends are expected according to nucleation theory. For example, in benzene, the $Au(PPh_3)Cl$ precursor can form nanoparticles, demonstrating the lack of kinetic control on the reduction process for PPh_3 , that is observed with the diphosphines. This is especially true in the presence of a strong reducing agent such as sodium borohydride^{64,66,67}. In these environments the formation of nascent, stable metal clusters and their growth is favored, hence the size selectivity is lost^{68–70}. However, a recent attempt was made to develop accurate models of the relative rates of formation and growth for PPh_3 -protected clusters by following the temporal change in the populations of different cluster nuclearities using a colorimetric assay⁶⁵. Pettibone and Reardon compared

Au-PPh₃ and Au-L³ dissolved in a MeOH/CHCl₃ mixture reduced with BTBC and NaBH₄ at 0°C and 20°C. The change in the reduction rate by change in temperature or reducing agent demonstrated the dependence on size distribution present in the Au-PPh₃ system, which is consistent with rate dependencies outlined in nucleation theory. In contrast, the evolution of the product distributions in the Au-L³ system were nearly identical irrespective of reducing agent and temperature, which demonstrates the control wielded by the diphosphine ligands in cluster formation⁷¹.

Size selectivity in Au MPCs has been reported to depend on several factors, including temperature (controlling reduction rates and secondary processing rates), time, solvent, and ligand length and flexibility. Theoretical calculations have shown that length and flexibility of spacer are critical for size selectivity as well as ligand-metal bond strength and verified by experiment⁸. However, these calculations do not include solvent effects. Besides changing the rates of metal reduction or solubility of the precursors and products, solvents can affect the solubility of the reaction products and, consequently, cluster size and monodispersity. For example, the bond between gold and diphosphines is stronger in polar solvents such as methanol and is weaker in solvents of moderate polarities for such as chloroform^{41,68,72}. Because the polar protic solvents have the ability to affect the metal-ligand interaction in ligand exchange reactions, they can alter the selectivity of different core sizes⁷².

In this paper, we examine the roles of length and flexibility of the aliphatic/alkyl chain of the diphosphine ligand and of solvent polarity on the distribution of ultrasmall Au MPC's.

To study the effect of the spacer on size selectivity, we selected diphosphine ligands with different lengths and rigidity, but with nearly identical electronic structure; the shortest chain $\text{PPh}_2(\text{CH}_2)\text{PPh}_2$, i.e., 1,1-bis(diphenylphosphino)methane, denoted by L^1 , two short chains $\text{PPh}_2(\text{CH}_2)_3\text{PPh}_2$, i.e., 1,3-bis(diphenylphosphino)propane, denoted by L^3 , and $\text{PPh}_2(\text{CH}_2)_4\text{PPh}_2$, i.e., 1,4-bis(diphenylphosphino)butane, denoted by L^3 , a long, flexible chain, $\text{PPh}_2(\text{CH}_2)_6\text{PPh}_2$ i.e., 1,6-bis(diphenylphosphino)hexane denoted by L^6 , two rigid ligands, 4,5-Bis(diphenylphosphino)-9,9-dimethylxanthene (xantphos) denoted by L^{Ar} , and 2,2'-bis(diphenylphosphino)-1,1'-binaphthyl (BINAP) denoted by L^{Bn} , and a moderately flexible spacer 2,2'-Bis(diphenylphosphino)biphenyl (Biphenyl) denoted by L^{Bp} (Figure 3.1). Furthermore we examined the effect of solvent on the core sizes of gold nanoclusters and on the stability of molecular ion complexes by altering the solution from polar to non-polar solvents:

Methanol (highest polarity) \rightarrow Ethanol \rightarrow Propanol \rightarrow Butanol \rightarrow CHCl_3 (lowest polarity)

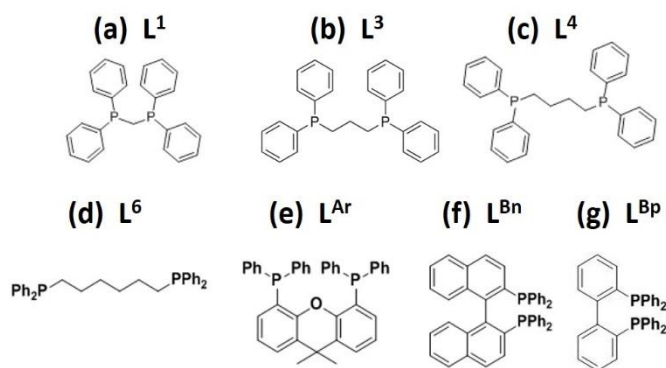


Figure 3.1: Pictures of:

- (a) 1,1-Bis(diphenylphosphino)methane
- (b) 1,3-Bis(diphenylphosphino)propane
- (c) 1,4-Bis(diphenylphosphino)butane
- (d) 1,6-Bis(diphenylphosphino)hexane
- (e) 4,5-Bis(diphenylphosphino)-9,9-dimethylxanthene (Xantphos) – rigid spacer
- (f) 2,2'-Bis(diphenylphosphino)-1,1'-binaphthyl (Binap)
- (g) 2,2'-Bis(diphenylphosphino)biphenyl

We observed that size selectivity was achieved with our most flexible ligands, L³ and L⁶. The more rigid ligands displayed short-term selectivity only in the smallest solvents, chloroform and methanol, which also happen to be the least and most polar. This indicates that the size of the solvent plays an important role in the formation of MPC's.

3.2 Results and discussion

In this section we present the effects of different reaction variables on the size selectivity of MPCs in deaerated solutions. The effect of spacer length, solvent and reaction time are studied using UV-Visible spectra and electrospray ionization mass spectrometry (ESI-MS) and a comparison is made. It has been shown that the reduction of Au ions and growth of Au clusters is slow when Borane *tert*-butylamine (BTBC) is employed as the reducing agent⁶¹. This slow growth allowed us to monitor the change in the mean cluster size of a suspension with increasing reaction time.

3.2.1 L¹ Au Clusters

The UV-Visible spectrum (Figure 3.2) exhibits multiple broad absorption peaks around 525 nm and 440 nm in methanol, ethanol and butanol while no apparent peaks are shown in chloroform. Corresponding ESI-MS shown in Figure 3.3 indicate the formation of primarily Au₂₋₄ clusters with the exception of in butanol where we see Au₉ cores, specifically we see [Au₉(L¹)₅]³⁺ and [Au₉(L¹)₅Cl]²⁺ at 1231 m/z and 1864 m/z respectively. These results are consistent to that previously reported by Pettibone and Hudgens⁶⁴ for L¹ in a chloroform/methanol mixture where we see predominately Au_xL₂ complexes, with $x = 1-3$. Long-term UV-Vis analysis of our solutions indicate the instability of our shortest and rigid spacer, demonstrating its lack of selectivity.

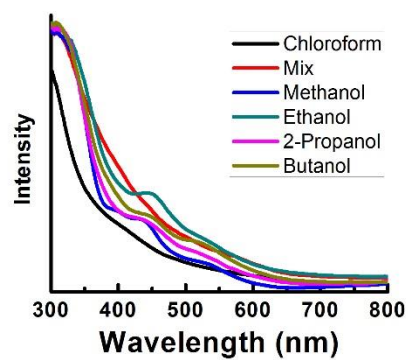


Figure 3.2: UV-Visible Spectroscopy of Au:L¹

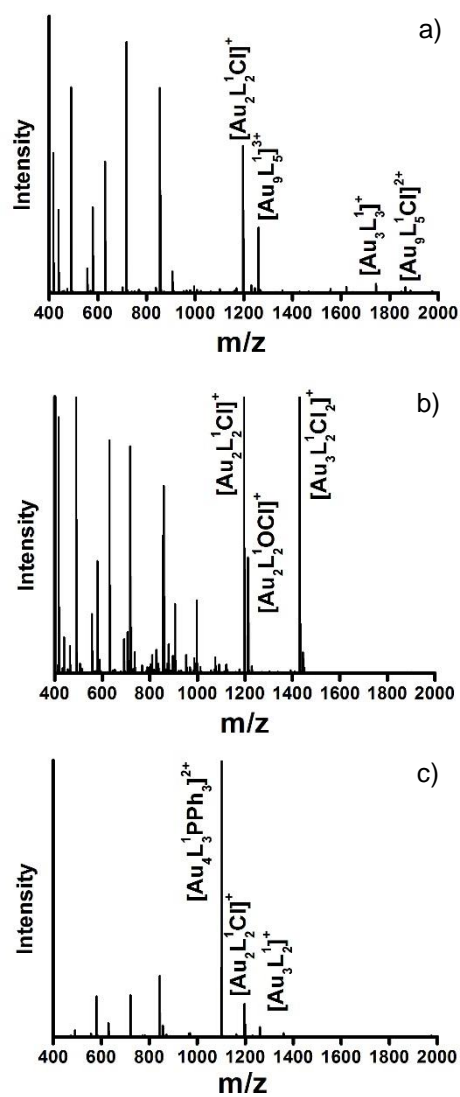


Figure 3.3: ESI-MS of L¹ in a) butanol, b) chloroform and c) methanol

3.2.2 L^3 Au Clusters

The UV-Visible spectrum (Figure 3.4) shows an absorption peak at 420 nm corresponding to Au_{10} and Au_{11} clusters and is present for all solvents used⁴². The absorption peak is observed in all solvents, indicating the strong selectivity of L^3 . ESI-MS analysis in $CHCl_3$ (Figure 3.5) exhibit an intense peak at 1409 m/z which is indicative of $[Au_{11}(L^3)_5]^{3+}$ and is consistent with previous studies⁴². ESI-MS also shows strong peaks at 1020.5, 871 and 609 m/z which derive from the precursors $[Au(L^3)_2]^+$, $[Au(L^3)PPh_3]^+$ and $[Au_2(L^3)_2]^{2+}$ respectively⁶⁴.

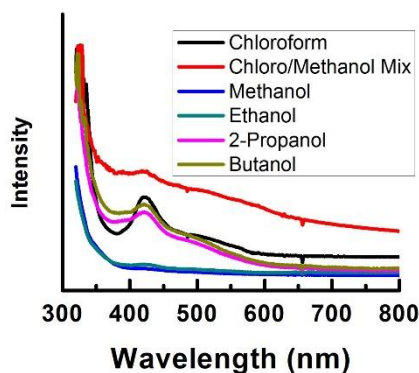


Figure 3.4: UV-Visible Spectroscopy of Au: L^3 . The 420 nm peak is present in all solvents indicating the formation of Au_{11} and the size selective behavior of L^3

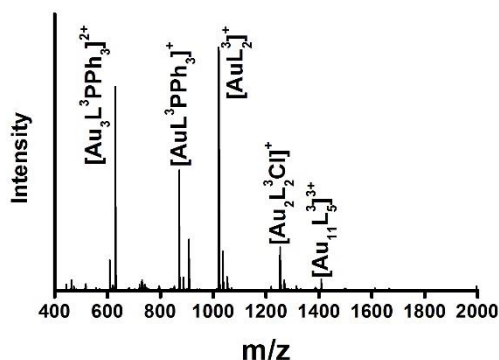


Figure 3.5: ESI-MS of Au: L^3 showing Au_{11} along with smaller gold complexes prepared in chloroform.

3.2.3 L⁴ Au Clusters

L⁴ also exhibits a very distinct absorption peak centered at 420 nm in all solvents used, which is similar to what was observed in L³ (Figure 3.6). UV-Vis study shows that this peak is stable indicating the long-term stability of L⁴. As previously stated, this absorption peak corresponds to the formation of Au₁₀ clusters which are observed in the ESI-MS. Figures 3.7 and 3.8, show the formation of [Au₁₀(L⁴)₄PPh₃]²⁺ in all solvents and is consistent with previous reports for L⁴ in a chloroform/methanol mixture⁶⁴. Additionally in chloroform, we see [Au₈(L⁴)₄]²⁺ and [Au₁₂(L⁴)₅]³⁺ at 1640 m/z and 1498 m/z respectively, along with smaller clusters, AuPPh₃ at 459 m/z in butanol and Au(L⁴)₂ at 1049 m/z in methanol.

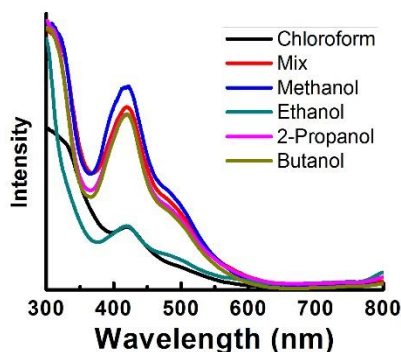


Figure 3.6: UV-Visible Spectroscopy of Au:L⁴

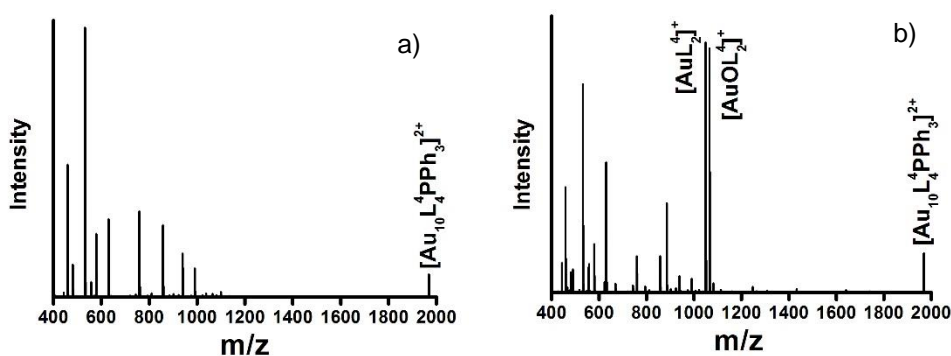


Figure 3.7: ESI-MS of L⁴ in a) butanol and b) methanol

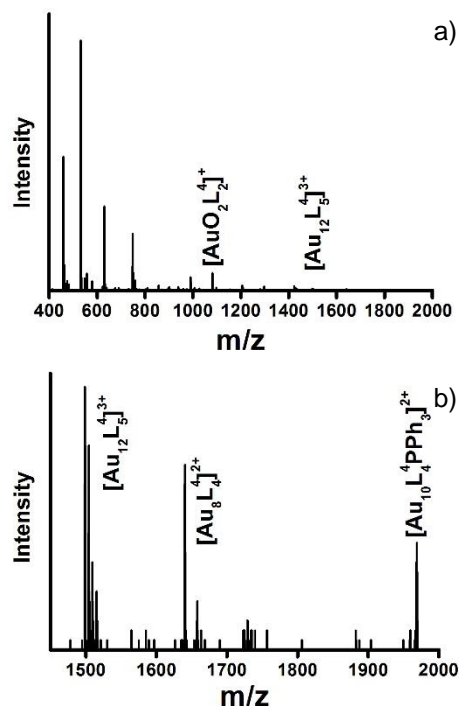


Figure 3.8: a) ESI-MS of L^4 in chloroform. b) An expanded view of L^4 in chloroform showing the 1450 m/z to 2000 m/z highlighting the Au_{12} , Au_{10} and Au_8 clusters.

3.2.4 L^6 Au Clusters

The use of L^6 in $CHCl_3$ has been shown to exhibit two predominant UV-Vis peaks at 411 and 430 nm which can be reconciled with Au_8 and Au_{10} , respectively⁴². Additionally, Pettibone and Hudgens showed that monodispersity can be achieved in a 1:1 chloroform/methanol solution by adjusting the ratio of L^6/PPh_3 ⁶². They report that at a ratio = 1 (as used in this study) the Au_8^{2+} and Au_{10}^{2+} cores initially seen, evolve into monodisperse $[Au_8(L^6)_4]^{2+}$ in 6 days and to $[Au_9(L^6)_4Cl]^{2+}$ in 14 days. Analyses of our work in these solvents show comparable results. The UV-Vis spectra for the chloroform-methanol mix has an absorption peak at 414 nm and a shoulder at 476 nm which is indicative of $[Au_{10}(L^6)_5]^{2+}$ and $[Au_8(L^6)_4]^{2+}$ (Figure 3.9-3.11). However, we observe an

absorption peak centered at 545 nm and a shoulder at ~680 nm for ethanol, propanol and butanol indicating growth and formation of nanoparticles. These results indicate a strong influence of solvent type on the dispersity of the suspensions. The formation of small clusters was observed only in CHCl_3 and methanol, which are the least and most polar solvents used, respectively. Coincidentally, they are also the smallest solvents employed indicating that polarity of solvent does not play an important role while solvent size does in determining size selectivity.

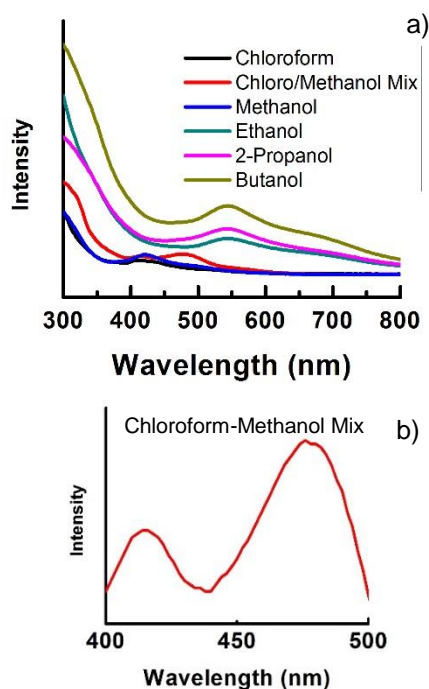


Figure 3.9: a) UV-Visible Spectroscopy of Au:L⁶. b) An expanded view of the chloroform and methanol mix showing the 414 nm and 476 nm peaks corresponding to Au₁₀ and Au₈, respectively.

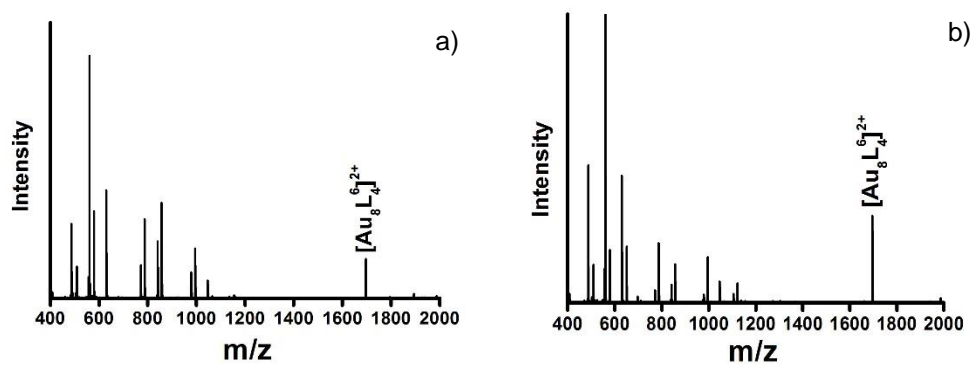


Figure 3.10: ESI-MS of L^6 in a) butanol and b) methanol

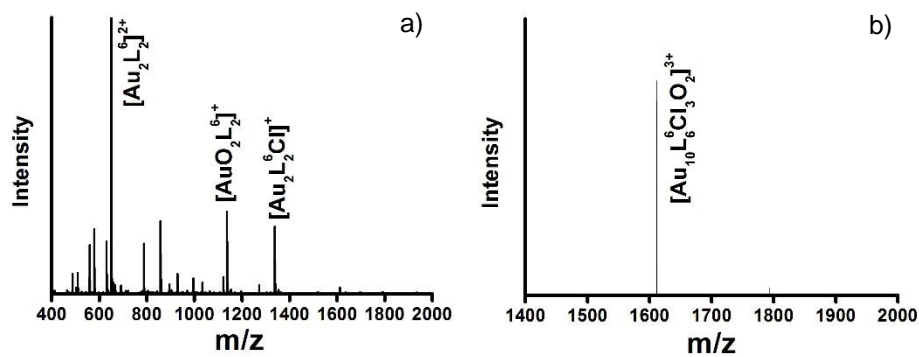


Figure 3.11: a) ESI-MS of L^6 in chloroform. b) An expanded view of L^6 in chloroform showing the 1400 m/z to 2000 m/z highlighting the Au_{10} cluster.

3.2.5 L^{Ar} (Xantphos) Au Clusters

Analysis of our UV-Visible spectra (Figure 3.12) shows possible size selectivity in CHCl₃ and in the CHCl₃/Methanol mixture with absorption peaks around 420 nm, which is consistent with the presence of Au clusters. ESI-MS analysis of clusters reveal two prominent peaks seen in all solvents tested. One at 1038 m/z and the other at 1355 m/z corresponding to [Au(L^{Ar})PPh₃]⁺ and [Au(L^{Ar})₂]⁺ respectively (Figure 3.13). Long-term UV-Vis and MS show the instability of L^{Ar} as can be seen in figures 3.14 and 3.15. These results indicate our most rigid spacer, xantphos, does not bind to form stable Au clusters.

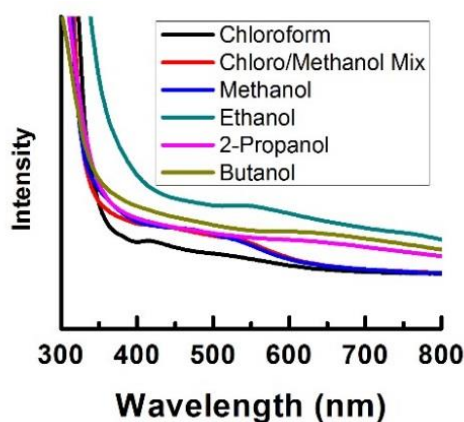


Figure 3.12: UV-Visible Spectroscopy of Au:L^{Ar}.

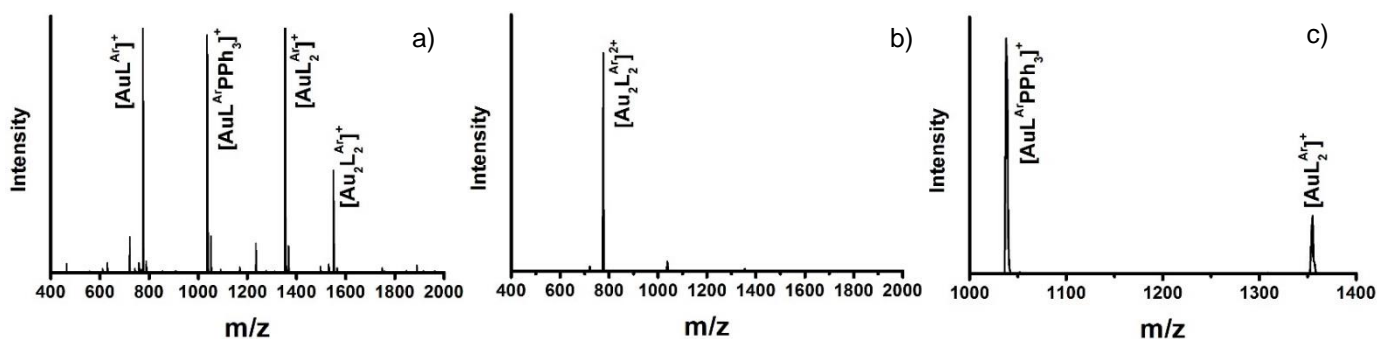


Figure 3.13: ESI-MS of L^{Ar} (Xantphos) in Chloroform a) and Methanol b) and c).

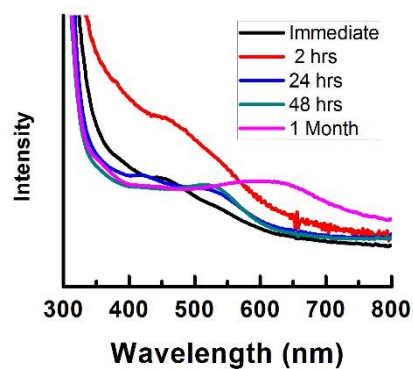


Figure 3.14: Time study of UV-Visible Spectroscopy of Au:L^{Ar} showing the instability of Xantphos.

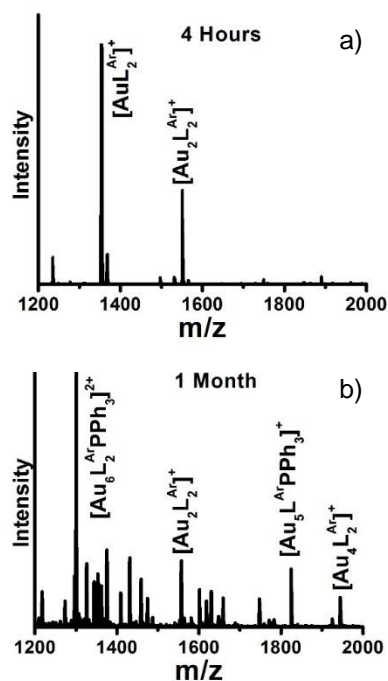


Figure 3.15: ESI-MS of L^{Ar} (Xantphos) in chloroform a) immediate (< 4 hrs) and b) 1 month old sample showing the lack of size selectivity and instability of Xantphos.

3.2.6 L^{Bn} (BINAP) Au Clusters

We see distinct peaks at 370 nm and 420 nm in the UV-Vis spectra in CHCl₃/Methanol mixture and methanol, which resembles previously reported spectra by Yanagimoto *et al*⁷³. In all other solvents we see a broad absorption band at larger wavelengths as shown in Figure 3.16. Long term ($t > 48$ hrs) we observe the formation of Au nanoparticles which are indicated by the development of precipitates and plating on the glass vial. The ESI-MS in methanol and chloroform (figure 3.17) indicates two strong peaks; one at 1443 m/z which is attributed to [Au₁₀(PPh₃)₉]³⁺, and the other at 1081 m/z for [Au(L^{Bn})PPh₃]⁺ which is again consistent with our UV-Visible spectra absorption peaks centered at 420 nm for methanol and less intense peaks at 380 nm and 430 nm for chloroform. Additionally, in figure 3.17, we observed mixed BINAP/PPh₃ and Chlorinated/PPh₃ ligated clusters. For example in CHCl₃ (a), a 1313 m/z is attributed to [Au₉(PPh₃)₈Cl₂]³⁺, and in methanol (b) we see 1081 m/z for [Au(L^{Bn})PPh₃]⁺. Compared to Xantphos, BINAP exhibits a somewhat improved ability to bind to form Au clusters. The suspensions, however, are not stable and therefore result in poor size selectivity.

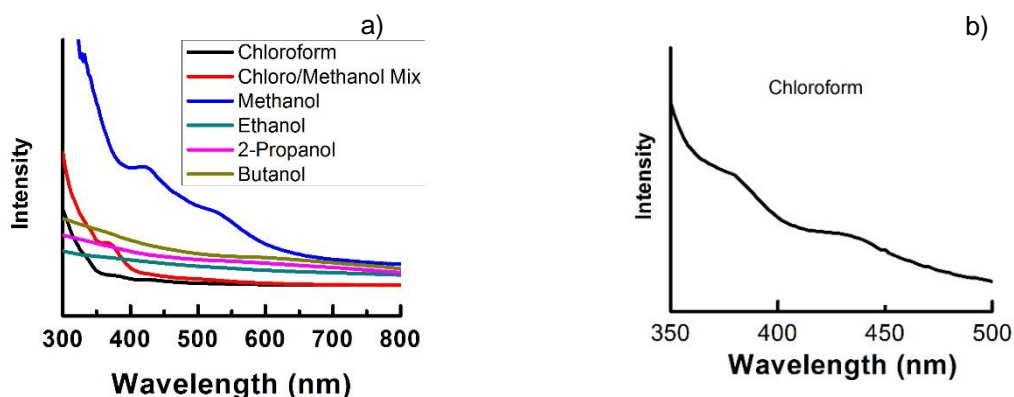


Figure 3.16: UV-Visible Spectroscopy of Au:L^{Bn}. On the right is an expanded view of chloroform showing the 380 nm and 430 nm peaks corresponding to Au₉ and Au₁₀, respectively.

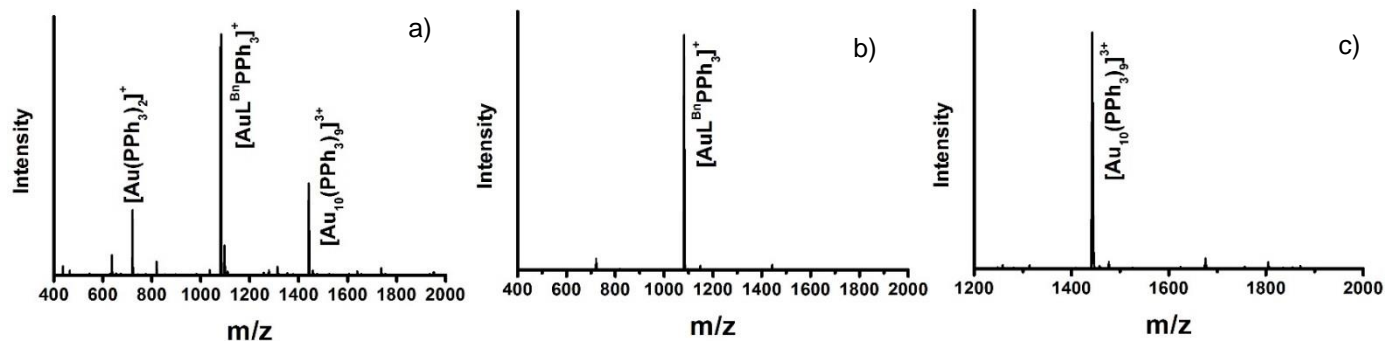


Figure 3.17: ESI-MS of L^{Bn} in Chloroform a) and Methanol b) and c). Expanded view in Methanol c).

3.2.7 L^{Bp} (Biphenyl) Au Clusters

The UV-Visible spectra (Figure 3.18) in chloroform, methanol, ethanol and the mixture of chloroform and methanol all exhibit at least one peak in the 400-420 nm region. The narrowest absorption is for chloroform which suggests the formation of Au_{10} clusters and is confirmed by a 1353 m/z peak for $[Au_{10}(PPh_3)_8]^{3+}$ in MS (Figure 3.19). $[Au_7(PPh_3)_7Cl]^{3+}$ and $[Au_{10}(PPh_3)_9]^{3+}$ strong peaks are observed in methanol which would explain the absorption peaks at 420 nm. In butanol, $[Au(L^{Bp})_2]^+$, $[Au_3(L^{Bp})_2]^+$, and $[Au_8(PPh_3)_7]^{2+}$ MS peaks are prominent, along with a polydisperse mixture produced with biphenyl and/or PPh_3 ligated clusters. This polydispersity might explain the broad absorption peaks observed in the UV-Visible spectra. Biphenyl, a slightly more flexible ligand than L^{Ar} and L^{Bn} , shows the formation of polynuclear ligated clusters and confirms the importance of ligand flexibility in determining selectivity. However, similar to BINAP, suspensions containing biphenyl quickly precipitate and form a film in all solvents.

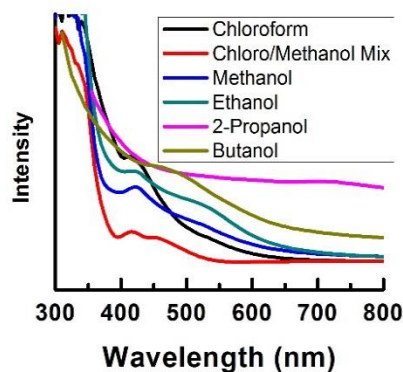


Figure 3.18: UV-Visible Spectroscopy of Au:L^{Bp}

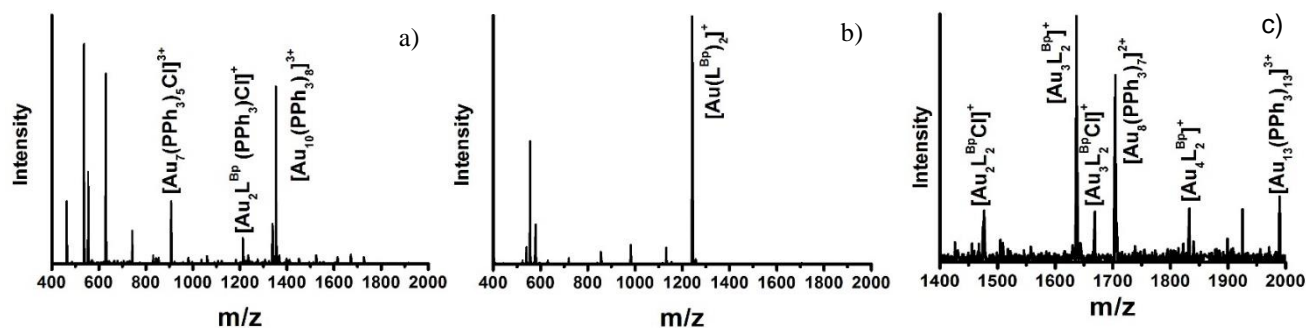


Figure 3.19: ESI-MS of L^{Bp} in Chloroform a) and Butanol b) and c). Expanded view in Butanol c).

3.3 Experimental

In a typical synthesis, AuPPh₃Cl was dissolved in a glass vial in the solvent of choice to reach a concentration of 10⁻³ M. The desired ligand was then added in equal molarity and solution was sonicated until completely dissolved, occasionally bubbling Ar gas through then continue sonicating. Lastly, BTBC is added at a concentration of 5×10⁻³ M and sonicated again for about 30 min, while regularly bubbling Ar gas to remove dissolved oxygen from solutions.

3.3.1 Measurements

Mass spectrometric analysis was carried out using a Linear Ion Trap Quadrupole mass analyzer (QTRAP 6500 High Mass-1, AB SCIEX, Foster Hill, CA). Samples were introduced to the mass analyzer at a rate of 5 microliters/minute diluted 10 fold in methanol. All analysis were carried out in the positive ionization mode and the ionization parameters were as follows; DP = 60, EP=10, GS1 at 10 PSI, Curtain Gas = 20 PSI, Source Temperature at 60 C and ion spray voltage (IS) of 5500. Data were acquired in the MS mode for either 1 minute, beginning one minute after stabilization of the total ion current. All lines were flushed with 1 ml of methanol in between samples and the sample carryover was negligibly small (<0.1%) under these conditions. UV-Visible Spectra was taken with an Ocean Optics USB-2000 UV-Visible Spectrometer.

3.4. Conclusions

We have shown that stability and size selectivity of diphosphine ligated gold clusters is dependent on size and flexibility/rigidity of spacer groups and is not strongly dependent on the solvent. UV-Visible spectroscopy and Electrospray Ionization Mass spectrometry results revealed that the small flexible spacer (bis(diphenylphosphino)propane/ L^3) exhibits the greatest size selectivity towards cluster formation of smaller core sizes in all solvents used. Additionally, we have shown that the L^3 , L^4 and L^6 systems are stable for longer time periods (> 2 weeks), whereas the L^{Ar} , L^{Bn} and L^{Bp} systems are not. Suspensions prepared using these latter ligands typically exhibit ESI-MS peaks of small Au clusters bound to PPh_3 and not to diphosphines. The only exception is biphenyl, which can bind to Au clusters of small nuclearity. Short-term selectivity, limited to PPh_3 -capped clusters, tends to be higher for solvents made by small molecules. Solvent polarity does not seem to play

a role since the highest selectivity was achieved in chloroform and methanol, which are the lowest and highest polarity, respectively. These suspensions are not stable, and over time, nanoparticles form and plate the glass vial or precipitate out of solution. We have also shown how UV-Visible spectroscopy can be used for quickly identifying gold core sizes by their absorption peaks, which lead to apparent selectivity, however we have seen with ESI-MS that the absorption peaks may arise from nanoclusters bound to PPh_3 and not to diphosphines.

Further studies investigating other reaction conditions such as pH, time dependence, more geometrically related ligands and exploration of mechanism are our future interests so that control over size selectivity in Au cluster formation may be achieved.

CHAPTER 4 Synthesis of Diphosphine Ligated Au₈ and Au₁₄ Nanoclusters

4 Synthesis of Diphosphine Ligated Au₈ and Au₁₄ Nanoclusters

4.1 Introduction

Interest in gold nanoclusters of specific size and structure has been growing rapidly over the past few decades. Gold nanoclusters exhibit optical properties that make them excellent candidates for applications such as data storage, ultrafast switching and gas sensing^{42,55}. Additionally, they have the potential to be utilized in drug delivery systems, cancer therapy and the treatment of Alzheimer's disease, as well as their use in catalysis^{8,10–12,15,37,57,74}. Common techniques utilized in Au cluster formation result in polydisperse suspensions. Monodispersity can be achieved through the addition of ligands, typically the use of thiols due to the strong Au-S bond^{4,6}. However recently, diphosphine based ligands have gained considerable attention due to their size selectivity and simplified processing.

Bertino et. al. demonstrated a single phase one pot scheme to achieve ultra-small Au clusters. Their method involved dissolving Chloro(triphenylphosphine)gold(I) and a diphosphine ligand (PPh₂(CH₂)_MPPh₂) in an organic solvent with the addition of borane-*tert*-butylamine complex (BTBC) as the reducing agent. The effect of varying the aliphatic chain length, M, on size selectivity has been studied for the M = 1, 3-5, 6 and 10 ligands^{8,41,42,62,75}. Results show that flexibility of the spacer ligand is key in the formation of ultra-small ligated Au clusters and that size selectivity was achieved with the small spacer, M = 3.

The crystal structures of many small gold clusters has been extensively studied, specifically, the Au₈ core we see here⁷⁶. However, very little has been reported on the Au₁₄ structure. The Au₈ structure has been studied previously by Kamei, Shichibu and Konishi^{40,76}. For their synthesis they used a growth based strategy starting with [Au₆L³₄](NO₃)₂, whose core

contains a Au₄ tetrahedral unit with 2 gold atoms at each edge, and through a reaction with chloro-gold (I) complex [Au(PPh₃)Cl], yielded the [Au₈L³₄Cl₂]²⁺ cluster.

The Au₁₄ cluster is of particular interest due to the fact that geometrically and electronically we would expect the Au₁₃ cluster^{77,78}. Additionally, there have been many theoretical studies on Au₁₄, however there is very little done experimentally to show the formation of a ligand protected Au₁₄ core^{11,78–81}. A ligand-stabilized [Au₁₄(PPh₃)₈(NO₃)₄](MeOH)₆ cluster was reported by Gutrath, which is stable at ambient conditions and whose single crystal structure was examined using X-ray diffraction and verified by DFT calculations⁷⁷. Additionally, Shichibu et. al. mention the formation of a similar [Au₁₄L²₅Cl₄]²⁺ cluster when [Au₁₃L²₅Cl₂]³⁺ treated with HCl in ethanol and dichloromethane^{82,83}.

This study reports the formation of stable chlorinated diphosphine ligated Au₈ and Au₁₄ clusters using the PPh₂(CH₂)₃PPh₂ ligand, denoted as L³. L³ was chosen due to its propensity toward monodispersity and because it has been shown to produce a stable [Au₁₁L³₅]³⁺ cluster. Utilizing the same procedure reported by Bertino et. al., but substituting potassium gold (III) chloride (KAuCl₄) for Au(PPh₃)Cl, we show that we can achieve a stable monodisperse suspension of ligated Au₁₁ clusters. Here we also report that with the addition of manganese (II) chloride tetrahydrate we observe that the Au₁₁ clusters disassociate and form stable Au₈ and Au₁₄ core clusters.

4.2 Experimental Section

We employed two different methods in the synthesis of our gold clusters and observed the same results in both cases indicating the versatility of this system. The two methods differ regarding the timing of the addition of the reducing agent. In the first case, the reducing agent was added to the Au precursor solution resulting in the formation of Au₁₁. After the cluster formation,

we then added the MnCl_2 to the solution. In the second case, we added the reducing agent to a solution of Au and Mn precursors. Mass spectrometry and absorption spectroscopy of suspensions prepared with the two methods coincided, suggesting that BTBC addition did not induce reduction of Mn^{2+} . This conjecture was confirmed by adding BTBC to a solution of MnCl_2 . No change in color was observed, indicating that the Mn precursor was not being reduced by BTBC.

Method 1: KAuCl_4 is dissolved into a 1:1 diethyl ether:methanol mixture to reach a concentration of 10^{-3} M. 1,3-bis(diphenylphosphino)propane, denoted by L^3 , is then added in equal molarity and the solution is sonicated until the reagents are completely dissolved. The reducing agent, borane tert-butylamine complex (BTBC) is then added in a concentration of 5×10^{-3} M. The solution is sonicated again for about 30 min while bubbling Ar gas. Once a dark brown color is reached, an aliquot is taken and MnCl_2 is added to the solution in a molar ratio of 1:7 Au:Mn.

Method 2: KAuCl_4 and MnCl_2 (1:7 molar ratio) are dissolved into a 1:1 diethyl ether:methanol mixture to reach a concentration of 10^{-3} M. L^3 was then added in equal molarity and the solution was sonicated until completely dissolved. BTBC is added at a concentration of 5×10^{-3} M and the entire solution is then sonicated again for about 30 min while bubbling Ar gas.

Characterization: Mass spectrometric analysis was carried out using a Linear Ion Trap Quadrupole mass analyzer (QTRAP 6500 High Mass-1, AB SCIEX, Foster Hill, CA). Samples were introduced to the mass analyzer at a rate of 5 microliters/minute diluted 10 fold in methanol. All analysis were carried out in the positive ionization mode and the ionization parameters were as follows; DP = 60, EP=10, GS1 at 10 PSI, Curtain Gas = 20 PSI, Source Temperature at 60 C and ion spray voltage (IS) of 5500. Data were acquired in the MS mode for either 1 minute, beginning one minute after stabilization of the total ion current. All lines were flushed with 1 ml of methanol in between samples and the sample carryover was negligibly small (<0.1%) under

these conditions. UV-Visible Spectra was taken with an Ocean Optics USB-2000 UV-Visible Spectrometer.

4.3 *Results and Discussion*

In our synthesis, we first prepare a suspension of monodisperse Au₁₁ clusters stabilized by a diphosphine ligand following an established procedure by Bertino et. al.⁴². MnCl₂ is then added to this suspension as previously stated, and over a time frame of two to three weeks the suspension changes color. Monitoring the suspension during this time with UV-Vis spectroscopy, Figure 4.1, shows a shift in the absorption peak. The peak at 420 nm, characteristic of Au₁₁, decreases in intensity, while an absorption peak at 505 nm increases in intensity. This shift in peak is attributed to the formation of the Au₈, Au₁₄ clusters^{40,65}.

Further investigation of the suspension with Electrospray Ionization Mass Spectrometry (ESI-MS) reveals the evolution of two prominent peaks at 1648 and 2480 m/z (Figure 4.2). These peaks have been identified as [Au₈L³₄Cl₂]²⁺ and [Au₁₄L³₅Cl₄]²⁺ respectively. Additionally, ESI-MS was taken 2 and 3 weeks after the addition of MnCl₂ and is shown in Figure 4.3, which reveals the evolution of the peak at 1648 m/z. This increase of the 1648 m/z peak intensity and decrease of the Au₁₁ signal suggests that the UV-Vis shift to the 505 nm absorption is correlated to the growth of the Au₈ and Au₁₄ clusters.

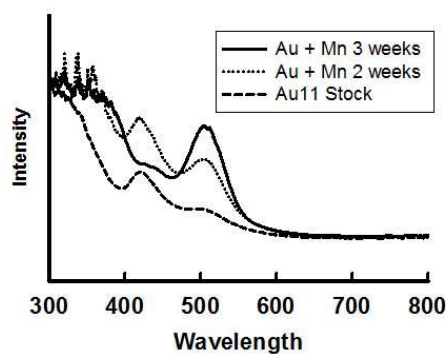


Figure 4.1: Optical absorption spectra of the parent Au₁₁ suspension and of the same suspension after addition of MnCl₂. The shift in peaks from 420 nm to 505 nm indicates the transformation of [Au₁₁L₅]³⁺ to [Au₈L₄Cl₂]²⁺ and [Au₁₄L₅Cl₄]²⁺.

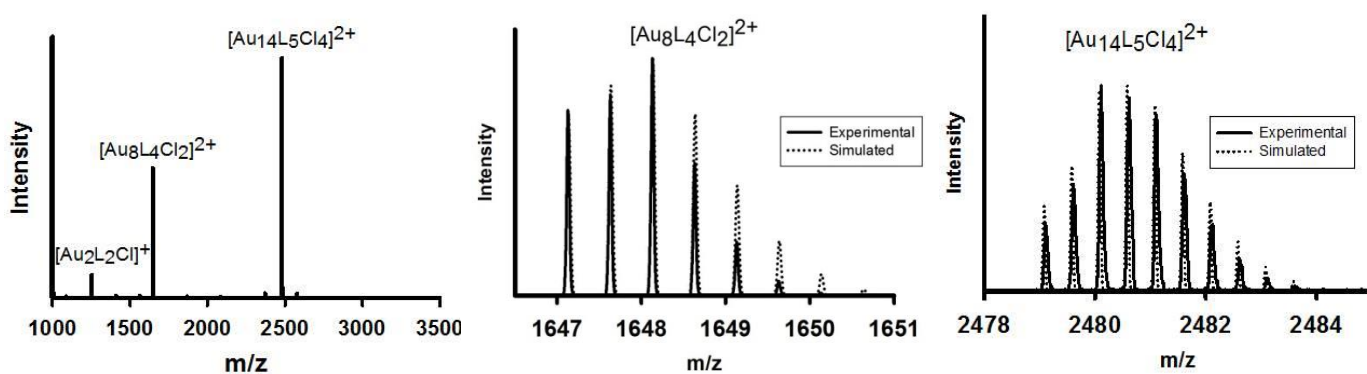


Figure 4.2: (Left) ESI-MS of our suspension after 3 weeks for [Au₈L₄Cl₂]²⁺ and [Au₁₄L₅Cl₄]²⁺. (Middle and Right) The experimental and simulated isotopic patterns of the Au₈ and Au₁₄ clusters.

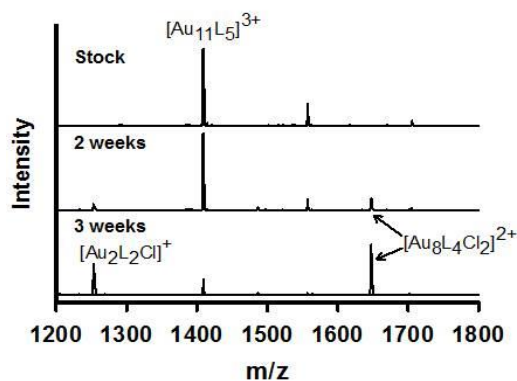


Figure 4.3: ESI-MS over 3-week period showing the growth of the 1647 m/z peak for Au₈.

4.4 Conclusion

The role of Mn in the corrosion of the Au₁₁L₅ cluster to the Au₈L₄Cl₂ and Au₁₄L₅Cl₄ is still unclear. However, we have shown a facile method to synthesize stable Au₈ and Au₁₄ diphosphine ligated clusters through the addition of MnCl₂ to a stable Au₁₁ suspension. Additionally, we have shown that this system is versatile and stable over long periods (>2 weeks). The role of Mn This method we use demonstrates a reproducible and modest approach in the development of exciting new gold nanoclusters.

4.5 Supporting Information

TEM analysis (Figure 4.S1a) shows relatively monodisperse particles with a size below 2 nm, and EELS analysis (Figure 4.S1b) of the area shows the presence of manganese. XPS analysis (Figure 4.S2) shows Au4f and Mn2p peaks at 84.9 eV and 642 eV, respectively, with a Mn satellite peak at ~647.4 eV. The satellite peak and the shift in binding energy for manganese indicate the formation of MnO. VSM measurements (Figure 4.S3) show paramagnetic behavior at room temperature and 50K (the lowest temperature accessible to our instrumentation), which is consistent with previous data for MnO¹⁰ and Au-Mn core-shell clusters. In all these systems, paramagnetic behavior is observed at temperatures larger than about 30 K. This varies from previously reported thiol and phosphine ligated gold nanoparticles where soft ferromagnetism is observed^{84,85}

4.5.1 Characterization

A Zeiss Libra 120 Transmission Electron Microscope (TEM) equipped with an Omega energy analyzer was used to acquire bright field micrographs and Electron Energy Loss Spectra

(EELS). Samples were prepared by placing drops of the suspensions onto a TEM grid. XPS was performed using a Thermo-Fisher Electron Spectroscopy for Chemical Analysis Lab 250 and binding energies were calibrated to C 1s peak at 284.8 eV. Information on magnetic properties was determined using a Quantum Design VersaLab Vibrational Sample Magnetometer (VSM). Samples were prepared by dropwise evaporation of suspensions onto a silicon substrate.

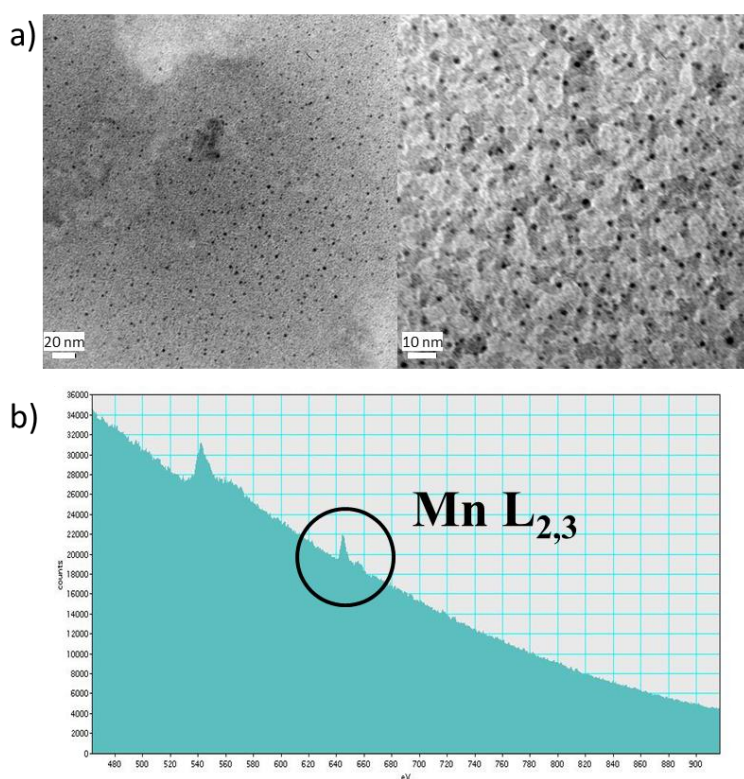


Figure 4.S1: a) Bright field micrographs showing the presence of aggregates with a diameter < 2 nm. b) EELS measurements showing peaks characteristic of Mn corresponding to the L_{2,3} edges. Au could not be measured by EELS because its lines lie outside the maximum energy accessible to our analyzer (1000 eV). The lines around 500 eV are characteristic of adventitious oxygen and are routinely encountered in samples analyzed with our microscope, including, for example, pure Au.

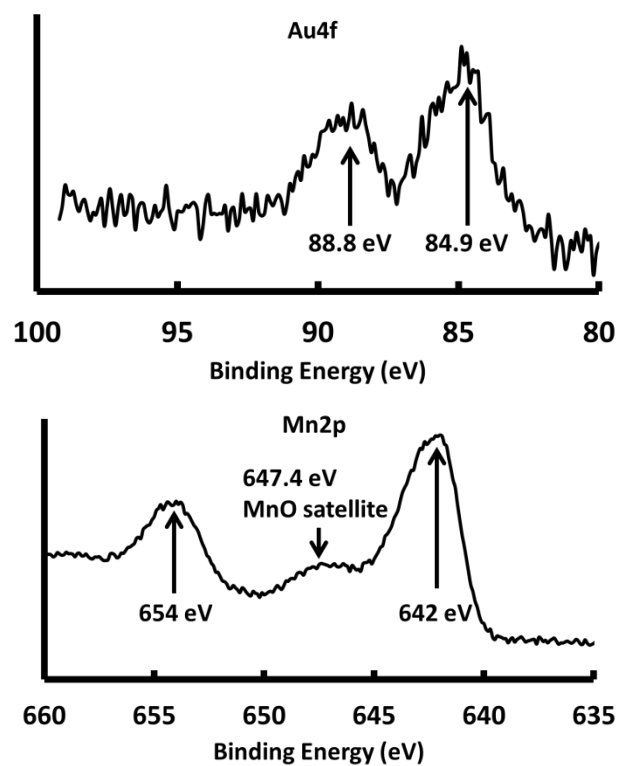


Figure 4.S2: XPS analysis of films produced by evaporation of the solution on silicon.

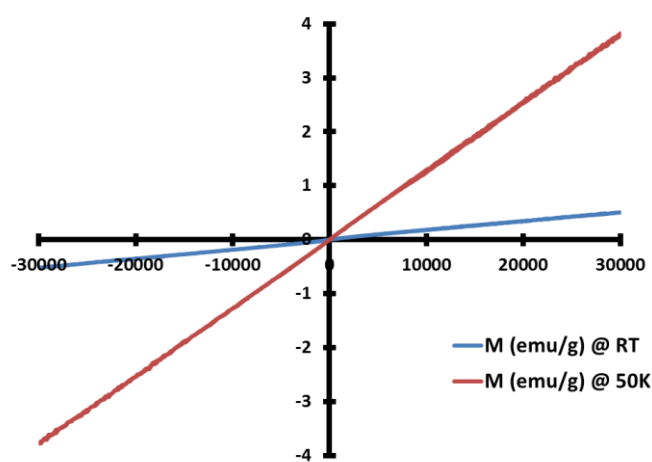


Figure 4.S3: VSM analysis of films produced by evaporation of the solution on silicon.

**CHAPTER 5 Novel Methods for the Synthesis of Monodisperse
Au₉ solutions and Au films through the addition of NiCl₂**

5 Novel Methods for the Synthesis of Monodisperse Au₉ solutions and Au films through the addition of NiCl₂

5.1 Introduction

The catalytic properties of gold date back into the 1920's when gold powder was shown to be an active catalyst for the hydrogenation of ethylene, and in the 1960's, Tetenyi and Schachter showed that gold catalyzes both the hydrogenation and dehydrogenation of cyclic hydrocarbons⁸⁶. More recently, the catalytic activity of gold nanoparticles has gained interest since Haruta et. al. reported on them in 1987⁸⁷. Since then the importance of bimetallic gold systems has also grown due to the fact that gold has shown to improve the activity of other transition metal catalysts as well as afford the opportunity of tunable nanocatalysts⁸⁸⁻⁹².

The gold-nickel system has important applications in catalysis and has shown to be a highly active CO oxidation catalyst^{87,92-94}. The formation of Au-Ni alloy nanoparticles has been difficult to achieve by common reducing metal salts procedures. Typically, high temperature annealing is required which leads to agglomeration and therefore larger particles and less effective catalysts. We have been able to produce a Au-Ni alloy through a co-reduction of Au and Ni ions to produce a film via electroless deposition and various lower temperature heating techniques. This paper presents a detailed look at a simple reduction method of gold and nickel precursors and the formation of a film followed by heating of the substrate by a TEM electron beam and through an XRD-HTK attachment. Additionally, through the production of the AuNi films, we have shown a simple approach to producing a monodisperse solution of triphenylphosphine ligated Au₉ clusters.

5.2 *Experimental Procedures*

In the production of films, Pettibone et al. modified the procedure previously reported by Bertino for Au₁₁ synthesis by eliminating the addition of the L³ ligand. Dissolving 10⁻³M of triphenylphosphine gold chloride (Au(PPh₃)Cl) in a 1:1 Diethyl Ether:Methanol solution and reducing with 5×10⁻³ M of Borane-tert-Butylamine complex (BTBC) ^{42,95}. By doing this, he observed the formation of a metallic film via electroless deposition of a PPh₃-protected Au₉ nanocluster. We modified this technique with the addition of NiCl₂, CoCl₂ and MnCl₂ and monitored them in solution and film formation using UV-Visible, TEM and XRD techniques. For the purposes of this report we are only discussing the effect of the addition of NiCl₂ on a known solution of Au nanoclusters. MnCl₂ and Au has been reported previously and CoCl₂ did not yield any significant products, however we believe it is still of particular future interest.

A second experiment we report here is using Au(PPh₃)Cl (or KAuCl₄) and NiCl₂ + 6H₂O dissolved into a 1:1 diethyl ether:methanol mixture to reach a concentration of 10⁻³ M. 1,3-bis(diphenylphosphino)propane, denoted by L³, is then added in equal molarity and the solution is sonicated until the reagents are completely dissolved. The reducing agent, borane tert-butylamine complex (BTBC) is then added in a concentration of 5×10⁻³ M. The solution is sonicated again for about 30 min while bubbling Ar gas.

5.3 *Results and Discussion*

In the making a AuNi alloy film through the co-reduction of Au and Ni precursors we observed two interesting results. First, we monitored the solution during the deposition. UV-Visible spectra for the solution shows two peaks at 420 nm and 520 nm (Figure 5.1b). This is consistent with previously reported Au_{8,9} cores and is verified in our mass spectrometry data ⁹⁵.

Figure 5.2 reveals an evolution of a $[\text{Au}_9(\text{PPh}_3)_8]^{2+}$ peak at 1935 m/z with the addition of NiCl_2 . A comparison with Figure 5.3 without Ni, shows that by adding Ni almost all precursors are removed yielding a monodisperse Au.

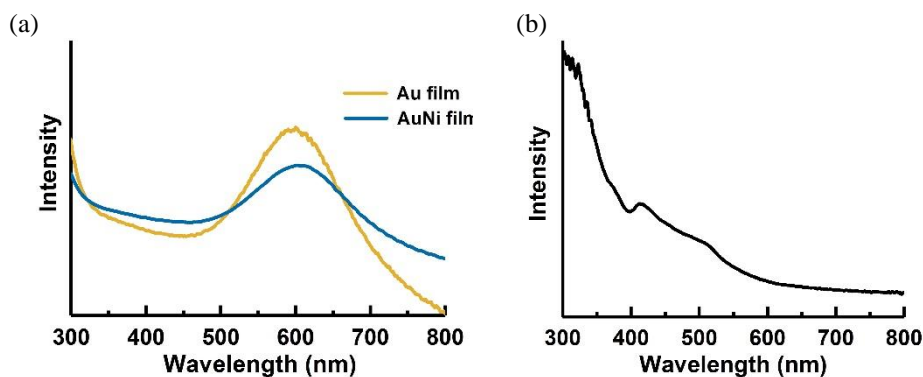


Figure 5.1: (a) UV-Vis spectra of gold film (yellow) and gold-nickel film (blue). Both have peaks at ~ 600 nm. (b) Shows UV-Vis for the Au:Ni solution. We can see a peak at 420 nm and one at 520 nm. This is consistent with Au_8 and Au_9 cores.

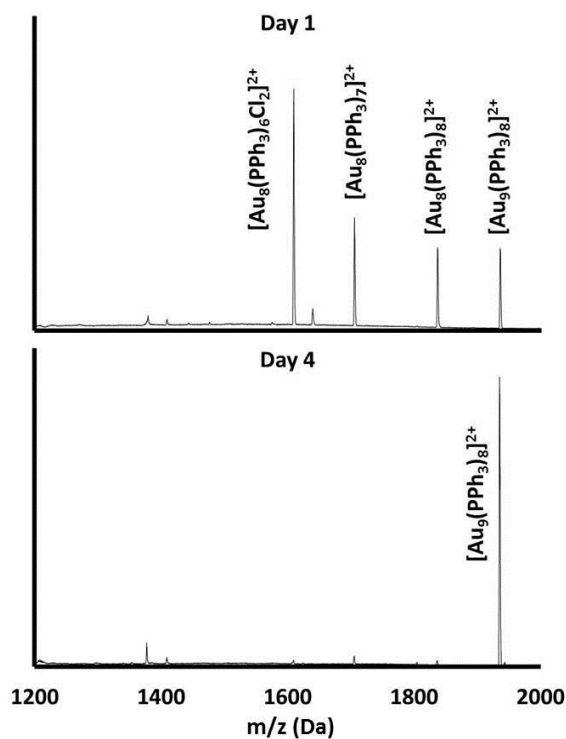


Figure 5.2: ESI-MS of the gold nickel solution after 1 day and 4 days reveals an evolution of the 1935 m/z peak.

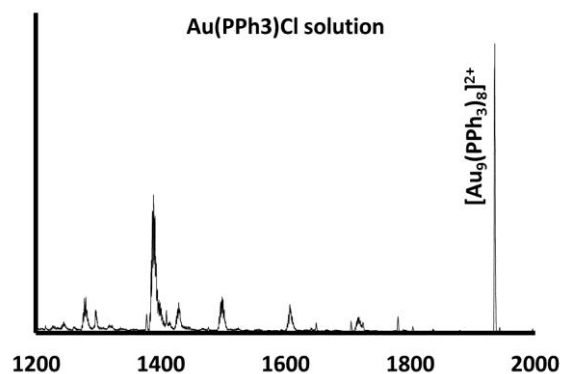


Figure 5.3: ESI-MS of the gold plating solution.

Second, we measured the properties of the film produced. Figure 1a shows the UV-Visible spectra of the films. We can see no discernable difference between the Au films and the Au films when Ni is added, and any difference could be attributed to film thickness ⁹⁵. The resistivity of the film was also measured at decreasing temperatures using an adapted VSM attachment. These measurements show an increase in resistivity with decreasing temperature. Resistivity's were measured to range from 0.1 – 2 $\Omega\cdot\text{m}$ at 300K – 50K respectively, which is what is expected and illustrates a Mott-Hubbard metal-insulator transition typical of a semiconductor (Table 5.1). We have observed that the nickel and gold precursors are being plated to the glass substrate. TEM and EELS analysis all confirm the presence of Ni in the films Figures 5.4,5.5. Additionally, we see that with low temperature heating we can achieve a AuNi alloy nanoparticles of around 20 nm in size figure (TEM). Also, XRD data shows the evolution of larger Au and Ni particles as the films are heated to 500 °C (fig. 5.6).

Table 5.1: Measurements of resistivity with decreasing temperature

Temperature (K)	300	250	200	150	100	50
Resistivity (Ωm)	0.14	0.16	0.19	0.24	0.40	1.98

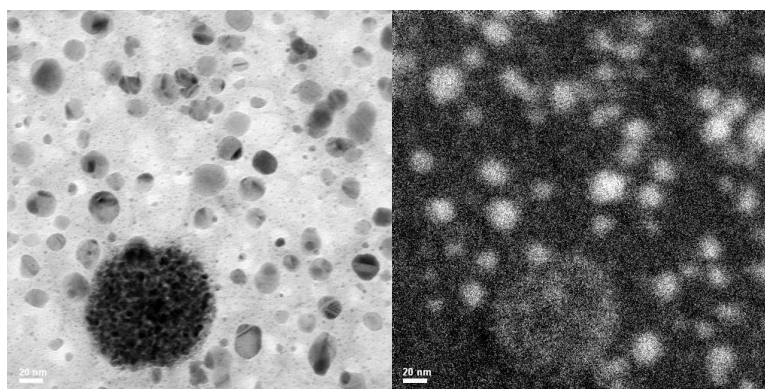


Figure 5.4: (left)TEM image of AuNi plated onto a grid. (right) TEM Nickel map. Scale bars are 20 nm.

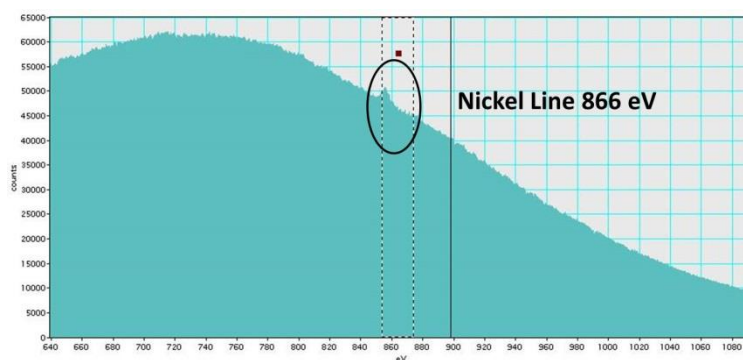


Figure 5.5: EELS of Nickel line

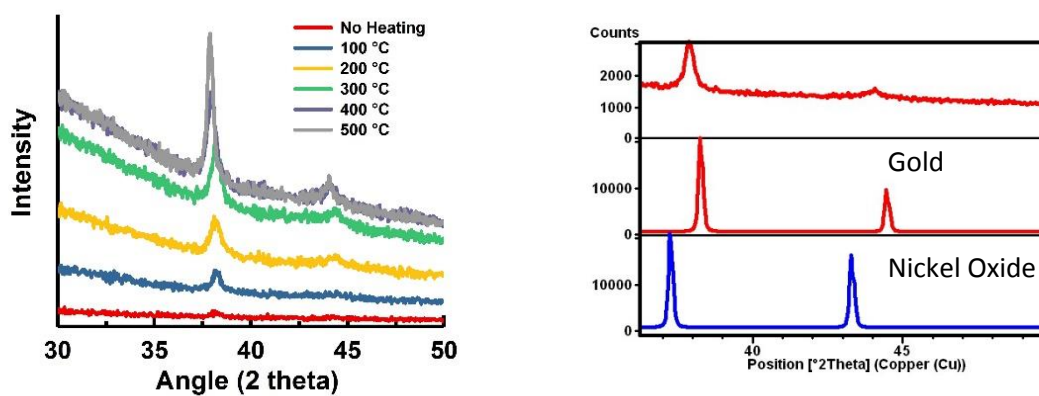


Figure 5.6: XRD showing the evolution of Au (38.1° and 44.3°), NiO (37.6° and 43.65°) and Ni (44.7°) peaks with increasing temperature (left). Comparison with Au and NiO (right)

We also report that the addition of NiCl_2 to a known solution of Au_{11} cores previously reported by Bertino et. al. using the L^3 ligand gave no new information⁴². Figure 5.7 shows the UV-Visible spectra for $\text{Au}(\text{PPh}_3)\text{Cl}$ and KAuCl_4 each with the addition of NiCl_2 . As can be seen, is a single peak at 420 nm, which is indicative of the formation of $[\text{Au}_{11}(\text{L}^3)_5]^{2+}$ cluster previously reported⁴².

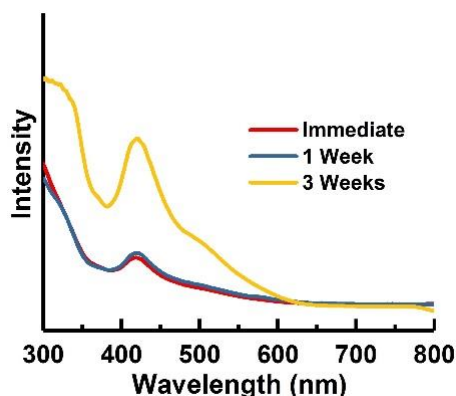


Figure 5.7: UV-Vis spectra of KAuCl_4 and NiCl_2 co-reduced with L^3 over time. We can see the 420 nm peak which we have shown is evidence of the Au_{11} cluster

5.4 Conclusion

The co-reduction of NiCl_2 and Au in the absence of the ligand (L^3) does give us a simple method for the production of a monodisperse $[\text{Au}_9(\text{PPh}_3)_8]^{2+}$ cluster solution and via electroless deposition does give us a potential low temperature pathway to the formation of a AuNi nanoalloy particle. Future work on this is to investigate the catalytic properties of these films as well as fine tuning the necessary conditions for in the formation of the Au-Ni nanoalloy clusters.

CHAPTER 6: Nanopore investigation of the *p*-mercaptobenzoic acid ligated gold nanocluster ($\text{Au}_x \text{ } p\text{-MBA}_y$)

6 Nanopore investigation of the *p*-mercaptobenzoic acid ligated gold nanocluster ($\text{Au}_x p\text{-MBA}_y$)

6.1 Introduction

Currently I am investigating the use of an alpha hemolysin (αHL) nanopore as a single particle detector to understand the kinetics of thiol ligated gold nanoclusters. This work has focused on the mercaptobenzoic acid (MBA) capped Au clusters, specifically the 4-MBA or *p*-MBA ligand. With the nanopore, we can observe small, discrete changes in current blockades, in real time, that correspond to changes in the molecular structure of the particle trapped in the pore. These changes vary with ligand. We chose to start with *p*-MBA due to the number of steps that were observed and the time scale over which these steps occur.

6.2 Methods

Looking for suitable, ~2 nm sized, water-soluble thiolate-protected gold nanoclusters that would work with our nanopore, we employed the Brust MPC synthesis of gold clusters outlined by Brust et. al.⁷ and Ackerson et. al.⁹⁶, focusing on the *p*-mercaptobenzoic acid (*p*-MBA) ligands and potassium gold (III) chloride (KAuCl_4). The synthesis of our $\text{Au}_x (p\text{-MBA})_y$ clusters was carried out in a single phase system in methanol. Potassium gold (III) chloride and *p*-mercaptobenzoic acid were dissolved in separate glass vials before being combined into one while stirring. A solution of borane *tert*-butylamine complex (BTBC) was then added with vigorous stirring. The solution was sonicated for at least 20 minutes until it turned dark brown, indicating the formation of a

polydisperse solution of our Au (*p*-MBA) clusters. The final concentrations of the KAuCl₄, *p*-MBA and BTBC were 1:1:5 mM respectively. Finally, we evaporated the methanol and rehydrated with DI water to for use with the nanopore.

6.3 Results

Figure 6.1 A shows a schematic of what the setup looks like with a tip filled with our sample of Au_x(*p*-MBA)_y nanoparticles positioned near the cis-side of the α HL pore. In a typical experiment, a voltage is applied, and after a 30 second delay a pump is turned on with a constant backing pressure to eject particles from the tip. The pump is turned off immediately after a particle is captured in the pore (red trace in fig 6.1 B). Figure 6.1 C shows a current blockade after a low pass filter has been applied revealing the step-like current events. Looking closer at the events (fig. 6.2A) we can count 10 steps and can see the discreteness of the steps in the histogram in figure 6.2 B, as well as the distribution of steps (fig 6.2C) indicating that these the events are caused by nearest state transitions or “next-nearest” state transitions.

6.4 Conclusions

This work is quickly becoming a new and exciting way to analyze water soluble Au clusters on a single particle, real time scale. The future direction of this research is to grow our knowledge on a variety of thiol protected Au nanoclusters, the benefit of Au for the moment is the extensive data that has already been collected, as well as look into other biologically relevant metals, such as iron oxide.

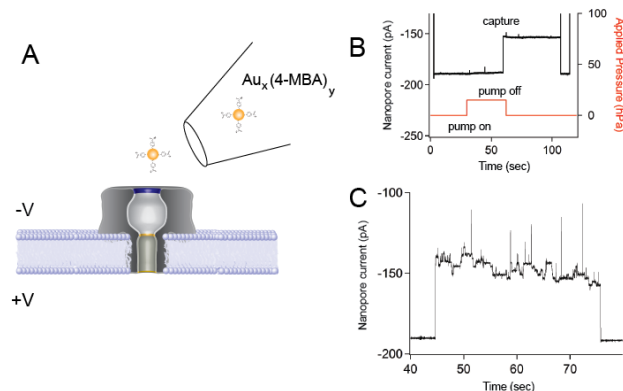


Figure 6.1: Schematic illustration of the experimental setup and a typical current trace for a single 4-MBA capped cluster trapped in the αHL pore. (A) A micropipette tip filled with a preformed sample of $\text{Au}_x(4\text{-MBA})_y$ nanoparticles is positioned near the cis-side entry of an αHL pore. (B) Time trace for a typical capture experiment shows that after applying a sufficient voltage and a 30-second delay, a constant backing pressure is applied to eject particles near the pore. Upon entry and capture of a particle into the pore, the current is reduced ca. 25% and the ejection pressure is immediately zeroed. (C) A low pass filter ($f_c = 100$ Hz) is used to extract step-like current noise indicative of events. Data shown was taken in 3M KCl at pH 7.2 under an applied 70 mV transmembrane potential.

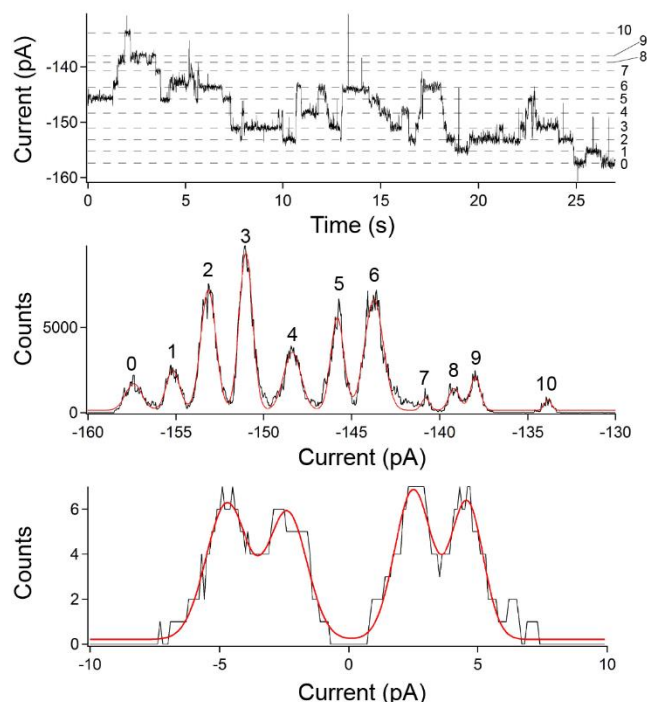


Figure 6.2: (A) Typical blockade current from a 4-MBA capped cluster shows discrete steps and ten clear substates. (B) An all-points histogram of this current identifies the quantized nature of the current states and the spacing shows a nearly linear dependence on the state and the steps. (C) The distribution of steps (transitions) between states shows that the events are caused by nearest state transitions or “next-nearest” state transitions.

Chapter 7: Summary

7 Summary

The purpose of this dissertation is to improve our understanding of ligated gold nanoclusters through ligand and solvent variation, as well as, with the addition of other metal salts and with the use of a nanopore.

We have shown that stability and size selectivity of diphosphine ligated gold clusters is dependent on size and flexibility/rigidity of spacer groups and is not strongly dependent on the solvent. UV-Visible spectroscopy and Electrospray Ionization Mass spectrometry results revealed that the small flexible spacer (bis(diphenylphosphino)propane/L³) exhibits the greatest size selectivity towards cluster formation of smaller core sizes in all solvents used. Additionally, we have shown that the L³, L⁴ and L⁶ systems are stable for longer time periods (> 2 weeks), whereas the L^{Ar}, L^{Bn} and L^{Bp} systems are not. Suspensions prepared using these latter ligands typically exhibit ESI-MS peaks of small Au clusters bound to PPh₃ and not to diphosphines. The only exception is biphenyl which can bind to Au clusters of small nuclearity. Short-term selectivity, limited to PPh₃-capped clusters, tends to be higher for solvents made by small molecules. Solvent polarity does not seem to play a role since the highest selectivity was achieved in chloroform and methanol, which are the lowest and highest polarity, respectively. These suspensions are not stable, and over time, nanoparticles form and plate the glass vial or precipitate out of solution. We have also shown how UV-Visible spectroscopy can be used for quickly identifying gold core sizes by their absorption peaks which lead to apparent selectivity, however we have seen with ESI-MS that the absorption peaks may arise from nanoclusters bound to PPh₃ and not to diphosphines.

We have shown a facile method to synthesize stable Au₈ and Au₁₄ diphosphine ligated clusters through the addition of MnCl₂ to a stable Au₁₁ suspension. Additionally, we have shown that this system is versatile and stable over long periods (>2 weeks). While the pathway is still under investigation, this method we use demonstrates a reproducible and modest approach in the development of exciting new gold nanoclusters.

The co-reduction of NiCl₂ and Au in the absence of the ligand (L³) does give us a simple method for the production of a monodisperse [Au₉(PPh₃)₈]²⁺ cluster solution and via electroless deposition does give us a potential low temperature pathway to the formation of a AuNi nanoalloy particle. Future work on this is to investigate the catalytic properties of these films as well as fine tuning the necessary conditions for in the formation of the Au-Ni nanoalloy clusters.

Lastly, we have investigated the kinetics of a Au_x (*p*-MBA)_y clusters trapped in an α-HL nanopore. The novel method illustrates the ability of the nanopore to be utilized as a single particle analytical tool for making real time measurements on the activity of our MBA capped gold clusters.

To summarize the implications of the studies in the previous chapters, a few points will be made. First, while gold nanoparticles have been studied extensively for many years, there is still much that we can learn about the system. More investigations into the role of ligand and solvent can be made to understand the conditions necessary for stable monodisperse solutions. Second, the addition of metal ions into well-established Au systems should be looked at closer to understand reaction pathways that lead to very interesting and strange results. Finally, the ability to monitor current fluctuations i.e. changes of state using a nanopore is exciting and an emerging analytical technique. Cluster analysis with a nanopore is not limited to gold and can easily be adapted for other metal nanoclusters.

REFERENCES

1. Daniel, M.-C. & Astruc, D. Gold Nanoparticles: Assembly, Supramolecular Chemistry, Quantum-Size-Related Properties, and Applications toward Biology, Catalysis, and Nanotechnology. *Chem. Rev.* **104**, 293–346 (2004).
2. Louis, C., Pluchery, Olivier. *Gold nanoparticles for physics, chemistry and biology*. (Imperial College Press, 2012).
3. Schmid, G. & Corain, B. Nanoparticulated Gold: Syntheses, Structures, Electronics, and Reactivities. *Eur. J. Inorg. Chem.* **2003**, 3081–3098 (2003).
4. Turkevich, J., Stevenson, P. C. & Hillier, J. A study of the nucleation and growth processes in the synthesis of colloidal gold. *Discuss. Faraday Soc.* **11**, 55 (1951).
5. Zhao, P., Li, N. & Astruc, D. State of the art in gold nanoparticle synthesis. *Coord. Chem. Rev.* **257**, 638–665 (2013).
6. Brust, M., Walker, M., Bethell, D., Schiffrin, D. J. & Whyman, R. Synthesis of thiol-derivatised gold nanoparticles in a two-phase Liquid?Liquid system. *J. Chem. Soc. Chem. Commun.* 801 (1994). doi:10.1039/c39940000801
7. Brust, M., Fink, J., Bethell, D., Schiffrin, D. J. & Kiely, C. Synthesis and reactions of functionalised gold nanoparticles. *J. Chem. Soc. Chem. Commun.* 1655 (1995). doi:10.1039/c39950001655
8. Hong, S., Shafai, G., Bertino, M. & Rahman, T. S. Toward an Understanding of Ligand Selectivity in Nanocluster Synthesis. *J. Phys. Chem. C* **115**, 14478–14487 (2011).
9. Li, J. Au₂₀: A Tetrahedral Cluster. *Science* **299**, 864–867 (2003).

10. Neely, A. *et al.* Ultrasensitive and Highly Selective Detection of Alzheimer's Disease Biomarker Using Two-Photon Rayleigh Scattering Properties of Gold Nanoparticle. *ACS Nano* **3**, 2834–2840 (2009).
11. Gao, Y., Shao, N., Pei, Y., Chen, Z. & Zeng, X. C. Catalytic Activities of Subnanometer Gold Clusters (Au_{16} – Au_{18} , Au_{20} , and Au_{27} – Au_{35}) for CO Oxidation. *ACS Nano* **5**, 7818–7829 (2011).
12. Bruchez Jr., M. Semiconductor Nanocrystals as Fluorescent Biological Labels. *Science* **281**, 2013–2016 (1998).
13. Cha, D. Surface reactivity of supported gold I. Oxygen transfer between CO and CO_2 . *J. Catal.* **18**, 200–211 (1970).
14. Parravano, G. Surface reactivity of supported gold II. Hydrogen transfer between benzene and cyclohexane. *J. Catal.* **18**, 320–328 (1970).
15. Haruta, M. Gold catalysts prepared by coprecipitation for low-temperature oxidation of hydrogen and of carbon monoxide. *J. Catal.* **115**, 301–309 (1989).
16. Haruta, M. Size- and support-dependency in the catalysis of gold. *Catal. Today* **36**, 153–166 (1997).
17. Ueda, A., Oshima, T. & Haruta, M. Reduction of nitrogen monoxide with propene in the presence of oxygen and moisture over gold supported on metal oxides. *Appl. Catal. B Environ.* **12**, 81–93 (1997).
18. Andreeva, D., Tabakova, T., Idakiev, V., Christov, P. & Giovanoli, R. Au/ α - Fe_2O_3 catalyst for water–gas shift reaction prepared by deposition–precipitation. *Appl. Catal. Gen.* **169**, 9–14 (1998).

19. Sakurai, H. & Haruta, M. Synergism in methanol synthesis from carbon dioxide over gold catalysts supported on metal oxides. *Catal. Today* **29**, 361–365 (1996).
20. Castleman, A. W. & Khanna, S. N. Clusters, Superatoms, and Building Blocks of New Materials [†]. *J. Phys. Chem. C* **113**, 2664–2675 (2009).
21. Claridge, S. A. *et al.* Cluster-Assembled Materials. *ACS Nano* **3**, 244–255 (2009).
22. Mandal, S. *et al.* Controlling the Band Gap Energy of Cluster-Assembled Materials. *Acc. Chem. Res.* **46**, 2385–2395 (2013).
23. Huang, X. & El-Sayed, M. A. Gold nanoparticles: Optical properties and implementations in cancer diagnosis and photothermal therapy. *J. Adv. Res.* **1**, 13–28 (2010).
24. Kang, B., Mackey, M. A. & El-Sayed, M. A. Nuclear Targeting of Gold Nanoparticles in Cancer Cells Induces DNA Damage, Causing Cytokinesis Arrest and Apoptosis. *J. Am. Chem. Soc.* **132**, 1517–1519 (2010).
25. *Reviews in Plasmonics 2010*. **2010**, (Springer New York, 2012).
26. Kothalawala, N., Lee West IV, J. & Dass, A. Size-dependent molecule-like to plasmonic transition in water-soluble glutathione stabilized gold nanomolecules. *Nanoscale* **6**, 683 (2014).
27. Häkkinen, H. The gold–sulfur interface at the nanoscale. *Nat. Chem.* **4**, 443–455 (2012).
28. Qian, H., Zhu, M., Wu, Z. & Jin, R. Quantum Sized Gold Nanoclusters with Atomic Precision. *Acc. Chem. Res.* **45**, 1470–1479 (2012).
29. Negishi, Y. *et al.* X-ray Magnetic Circular Dichroism of Size-Selected, Thiolated Gold Clusters. *J. Am. Chem. Soc.* **128**, 12034–12035 (2006).
30. Jin, R. Quantum sized, thiolate-protected gold nanoclusters. *Nanoscale* **2**, 343 (2010).

31. Zhu, M. *et al.* Reversible Switching of Magnetism in Thiolate-Protected Au₂₅ Superatoms. *J. Am. Chem. Soc.* **131**, 2490–2492 (2009).
32. Lu, Y. & Chen, W. Sub-nanometre sized metal clusters: from synthetic challenges to the unique property discoveries. *Chem. Soc. Rev.* **41**, 3594 (2012).
33. Weare, W. W., Reed, S. M., Warner, M. G. & Hutchison, J. E. Improved Synthesis of Small ($d_{\text{CORE}} \approx 1.5$ nm) Phosphine-Stabilized Gold Nanoparticles. *J. Am. Chem. Soc.* **122**, 12890–12891 (2000).
34. Chi, L. F. *et al.* Single-electron tunneling in Au₅₅ cluster monolayers. *Appl. Phys. Mater. Sci. Process.* **66**, S187–S190 (1998).
35. Zhang, H., Schmid, G. & Hartmann, U. Reduced Metallic Properties of Ligand-Stabilized Small Metal Clusters. *Nano Lett.* **3**, 305–307 (2003).
36. Chen, J., Zhang, Q.-F., Williard, P. G. & Wang, L.-S. Synthesis and Structure Determination of a New Au₂₀ Nanocluster Protected by Tripodal Tetraphosphine Ligands. *Inorg. Chem.* **53**, 3932–3934 (2014).
37. Li, J. Au₂₀: A Tetrahedral Cluster. *Science* **299**, 864–867 (2003).
38. Chen, J., Zhang, Q.-F., Bonaccorso, T. A., Williard, P. G. & Wang, L.-S. Controlling Gold Nanoclusters by Diphosphine Ligands. *J. Am. Chem. Soc.* **136**, 92–95 (2014).
39. Van der Velden, J. W. A. *et al.* Intermediates in the formation of gold clusters. Preparation and x-ray analysis of [Au₇(PPh₃)₇]⁺ and synthesis and characterization of [Au₈(PPh₃)₆I]PF₆. *Inorg. Chem.* **23**, 146–151 (1984).
40. Kamei, Y., Shichibu, Y. & Konishi, K. Generation of Small Gold Clusters with Unique Geometries through Cluster-to-Cluster Transformations: Octanuclear Clusters with Edge-sharing Gold Tetrahedron Motifs. *Angew. Chem. Int. Ed.* **50**, 7442–7445 (2011).

41. Bergeron, D. E., Coskuner, O., Hudgens, J. W. & Gonzalez, C. A. Ligand Exchange Reactions in the Formation of Diphosphine-Protected Gold Clusters. *J. Phys. Chem. C* **112**, 12808–12814 (2008).
42. Bertino, M. F., Sun, Z.-M., Zhang, R. & Wang, L.-S. Facile Syntheses of Monodisperse Ultrasmall Au Clusters. *J. Phys. Chem. B* **110**, 21416–21418 (2006).
43. Kasianowicz, J. J., Robertson, J. W. F., Chan, E. R., Reiner, J. E. & Stanford, V. M. Nanoscopic Porous Sensors. *Annu. Rev. Anal. Chem.* **1**, 737–766 (2008).
44. Bayley, H. & Martin, C. R. Resistive-Pulse Sensing From Microbes to Molecules. *Chem. Rev.* **100**, 2575–2594 (2000).
45. Finney, E. E. & Finke, R. G. Nanocluster nucleation and growth kinetic and mechanistic studies: A review emphasizing transition-metal nanoclusters. *J. Colloid Interface Sci.* **317**, 351–374 (2008).
46. Lalena, J. N., Cleary, D. A., Carpenter, E. E. & Dean, N. F. *Inorganic Materials Synthesis and Fabrication*. (John Wiley & Sons, Inc., 2008). doi:10.1002/9780470191576
47. Thanh, N. T. K., Maclean, N. & Mahiddine, S. Mechanisms of Nucleation and Growth of Nanoparticles in Solution. *Chem. Rev.* **114**, 7610–7630 (2014).
48. Polte, J. Fundamental growth principles of colloidal metal nanoparticles – a new perspective. *CrystEngComm* **17**, 6809–6830 (2015).
49. Bruins, A. P. Mechanistic aspects of electrospray ionization. *J. Chromatogr. A* **794**, 345–357 (1998).
50. Ho, C. S. *et al.* Electrospray ionisation mass spectrometry: principles and clinical applications. *Clin. Biochem. Rev.* **24**, 3–12 (2003).

51. Kebarle, P. & Verkerk, U. H. Electrospray: From ions in solution to ions in the gas phase, what we know now. *Mass Spectrom. Rev.* **28**, 898–917 (2009).
52. Taylor, G. I. & McEwan, A. D. The stability of a horizontal fluid interface in a vertical electric field. *J. Fluid Mech.* **22**, 1 (1965).
53. Rayleigh, Lord. XX. *On the equilibrium of liquid conducting masses charged with electricity.* *Lond. Edinb. Dublin Philos. Mag. J. Sci.* **14**, 184–186 (1882).
54. Williams, D. B. & Carter, C. B. *Transmission electron microscopy: a textbook for materials science.* (Springer, 2009).
55. Dass, A., Holt, K., Parker, J. F., Feldberg, S. W. & Murray, R. W. Mass Spectrometrically Detected Statistical Aspects of Ligand Populations in Mixed Monolayer Au₂₅L₁₈ Nanoparticles. *J. Phys. Chem. C* **112**, 20276–20283 (2008).
56. Lloret, P., Ybarra, G., Granell, P., Socolovsky, L. & Moina, C. Preparation and microscopic characterization of magnetite–gold mesoparticles with tunable morphology. *Nano-Struct. Nano-Objects* **4**, 9–14 (2015).
57. Chen, X., Huang, Y.-F. & Tan, W. Using Aptamer–Nanoparticle Conjugates for Cancer Cells Detection. *J. Biomed. Nanotechnol.* **4**, 400–409 (2008).
58. Neely, A. *et al.* Ultrasensitive and Highly Selective Detection of Alzheimer’s Disease Biomarker Using Two-Photon Rayleigh Scattering Properties of Gold Nanoparticle. *ACS Nano* **3**, 2834–2840 (2009).
59. Knoppe, S., Boudon, J., Dolamic, I., Dass, A. & Bürgi, T. Size Exclusion Chromatography for Semipreparative Scale Separation of Au₃₈(SR)₂₄ and Au₄₀(SR)₂₄ and Larger Clusters. *Anal. Chem.* **83**, 5056–5061 (2011).

60. Zhang, H., Wang, X., Zhang, K. & Teo, B. K. Functional Crystals: Search Criteria and Design Principles. *J. Solid State Chem.* **152**, 191–198 (2000).
61. Pettibone, J. M. & Hudgens, J. W. Reaction network governing diphosphine-protected gold nanocluster formation from nascent cationic platforms. *Phys. Chem. Chem. Phys.* **14**, 4142 (2012).
62. Pettibone, J. M. & Hudgens, J. W. Synthetic Approach for Tunable, Size-Selective Formation of Monodisperse, Diphosphine-Protected Gold Nanoclusters. *J. Phys. Chem. Lett.* **1**, 2536–2540 (2010).
63. Hudgens, J. W., Pettibone, J. M., Senftle, T. P. & Bratton, R. N. Reaction Mechanism Governing Formation of 1,3-Bis(diphenylphosphino)propane-Protected Gold Nanoclusters. *Inorg. Chem.* **50**, 10178–10189 (2011).
64. Pettibone, J. M. & Hudgens, J. W. Predictive Gold Nanocluster Formation Controlled by Metal-Ligand Complexes. *Small* **8**, 715–725 (2012).
65. Pettibone, J. M. & Hudgens, J. W. Gold Cluster Formation with Phosphine Ligands: Etching as a Size-Selective Synthetic Pathway for Small Clusters? *ACS Nano* **5**, 2989–3002 (2011).
66. Zheng, N., Fan, J. & Stucky, G. D. One-Step One-Phase Synthesis of Monodisperse Noble-Metallic Nanoparticles and Their Colloidal Crystals. *J. Am. Chem. Soc.* **128**, 6550–6551 (2006).
67. Mingos, D. M. P., Snee, T. & Zhenyang, L. Bonding models for ligated and bare clusters. *Chem. Rev.* **90**, 383–402 (1990).
68. Liu, X., Worden, J. G., Huo, Q. & Brennan, J. P. Kinetic Study of Gold Nanoparticle Growth in Solution by Brust-Schiffrin Reaction. *J. Nanosci. Nanotechnol.* **6**, 1054–1059 (2006).

69. Lo, C. F., Karan, K. & Davis, B. R. Kinetic Studies of Reaction between Sodium Borohydride and Methanol, Water, and Their Mixtures. *Ind. Eng. Chem. Res.* **46**, 5478–5484 (2007).
70. Davis, R. E., Bromels, E. & Kibby, C. L. **Boron Hydrides. III. Hydrolysis of Sodium Borohydride in Aqueous Solution.** *J. Am. Chem. Soc.* **84**, 885–892 (1962).
71. Pettibone, J. M. & Reardon, N. R. Nucleation products of ligated nanoclusters unaffected by temperature and reducing agent. *Nanoscale* **4**, 5593 (2012).
72. Toikkanen, O. *et al.* Solvent-Dependent Stability of Monolayer-Protected Au₃₈ Clusters. *J. Phys. Chem. Lett.* **1**, 32–37 (2010).
73. Yanagimoto, Y., Negishi, Y., Fujihara, H. & Tsukuda, T. Chiroptical Activity of BINAP-Stabilized Undecagold Clusters. *J. Phys. Chem. B* **110**, 11611–11614 (2006).
74. Li, L. *et al.* CO Oxidation on TiO₂ (110) Supported Subnanometer Gold Clusters: Size and Shape Effects. *J. Am. Chem. Soc.* **135**, 19336–19346 (2013).
75. Woodworth, P. H. *et al.* Synthesis of gold clusters with flexible and rigid diphosphine ligands and the effect of spacer and solvent on the size selectivity. *Nano-Struct. Nano-Objects* **7**, 32–40 (2016).
76. Konishi, K. Phosphine-Coordinated Pure-Gold Clusters: Diverse Geometrical Structures and Unique Optical Properties/Responses. in *Gold Clusters, Colloids and Nanoparticles I* (ed. Mingos, D. M. P.) **161**, 49–86 (Springer International Publishing, 2014).
77. Gutrath, B. S. *et al.* [Au₁₄(PPh₃)₈(NO₃)₄]: An Example of a New Class of Au(NO₃)-Ligated Superatom Complexes. *Angew. Chem. Int. Ed.* **52**, 3529–3532 (2013).

78. Häkkinen, H. *et al.* On the Electronic and Atomic Structures of Small Au_N⁺ (N = 4–14) Clusters: A Photoelectron Spectroscopy and Density-Functional Study. *J. Phys. Chem. A* **107**, 6168–6175 (2003).
79. Lechtken, A., Neiss, C., Kappes, M. M. & Schooss, D. Structure determination of gold clusters by trapped ion electron diffraction: Au₁₄⁺–Au₁₉⁺. *Phys. Chem. Chem. Phys.* **11**, 4344 (2009).
80. Gilb, S., Weis, P., Furche, F., Ahlrichs, R. & Kappes, M. M. Structures of small gold cluster cations (Au_n⁺, n < 14): Ion mobility measurements versus density functional calculations. *J. Chem. Phys.* **116**, 4094–4101 (2002).
81. Gao, Y. *et al.* Structural and electronic properties of uranium-encapsulated Au₁₄ cage. *Sci. Rep.* **4**, (2014).
82. Shichibu, Y., Suzuki, K. & Konishi, K. Facile synthesis and optical properties of magic-number Au₁₃ clusters. *Nanoscale* **4**, 4125 (2012).
83. Shichibu, Y. & Konishi, K. HCl-Induced Nuclearity Convergence in Diphosphine-Protected Ultrasmall Gold Clusters: A Novel Synthetic Route to “Magic-Number” Au₁₃ Clusters. *Small* **6**, 1216–1220 (2010).
84. Guerrero, E. *et al.* Magnetometry and electron paramagnetic resonance studies of phosphine- and thiol-capped gold nanoparticles. *J. Appl. Phys.* **107**, 064303 (2010).
85. Nealon, G. L. *et al.* Magnetism in gold nanoparticles. *Nanoscale* **4**, 5244 (2012).
86. Schwank, J. Catalytic gold: Applications of elemental gold in heterogeneous catalysis. *Gold Bull.* **16**, 103–110 (1983).
87. Haruta, M., Kobayashi, T., Sano, H. & Yamada, N. Novel Gold Catalysts for the Oxidation of Carbon Monoxide at a Temperature far Below 0 °C. *Chem. Lett.* **16**, 405–408 (1987).

88. Schwank, J. Gold in bimetallic catalysts. *Gold Bull.* **18**, 2–10 (1985).
89. Sinfelt, J. H. Catalysis by alloys and bimetallic clusters. *Acc. Chem. Res.* **10**, 15–20 (1977).
90. Nikolaev, S. A., Smirnov, V. V., Vasil'kov, A. Y. & Podshibikhin, V. L. Synergism of the catalytic effect of nanosized gold-nickel catalysts in the reaction of selective acetylene hydrogenation to ethylene. *Kinet. Catal.* **51**, 375–379 (2010).
91. Wang, A., Liu, X. Y., Mou, C.-Y. & Zhang, T. Understanding the synergistic effects of gold bimetallic catalysts. *J. Catal.* **308**, 258–271 (2013).
92. Molenbroek, A. M., Nørskov, J. K. & Clausen, B. S. Structure and Reactivity of Ni–Au Nanoparticle Catalysts. *J. Phys. Chem. B* **105**, 5450–5458 (2001).
93. Zhou, S. *et al.* In Situ Phase Separation of NiAu Alloy Nanoparticles for Preparing Highly Active Au/NiO CO Oxidation Catalysts. *ChemPhysChem* **9**, 2475–2479 (2008).
94. Khan, I. H. & Francombe, M. H. Structure and Oxidation of Thin Gold-Nickel Alloy Films. *J. Appl. Phys.* **36**, 1699 (1965).
95. Pettibone, J. M. *et al.* Surface mediated assembly of small, metastable gold nanoclusters. *Nanoscale* **5**, 6558 (2013).
96. Ackerson, C. J., Jadzinsky, P. D. & Kornberg, R. D. Thiolate Ligands for Synthesis of Water-Soluble Gold Clusters. *J. Am. Chem. Soc.* **127**, 6550–6551 (2005).